A coupled Eulerian interface capturing and Lagrangian particle method for multiscale simulation

Victor Chéron, Jorge César Brändle de Motta, Thibault Ménard, Alexandre Poux, Alain Berlemont

A coupled Eulerian interface capturing and Lagrangian particle method for multiscale simulation.

Victor Chéron[a], Jorge César Brändle de Motta[a,*], Thibault Ménard[a], Alexandre Poux[a], Alain Berlemont[a]

[a] *CNRS UMR 6614-CORIA, Rouen Normandie Université, Saint-Étienne-du-Rouvray, Normandie, 76801, France*

Abstract

A new Eulerian-Lagrangian coupling on a staggered fluid mesh is proposed to simulate multiscale atomization. This coupling relies on a sharp interface capturing method (ICM) to transport the resolved fluid structures and a Lagrangian tracking algorithm to model the under-resolved Eulerian droplets. The Lagrangian droplets momentum is spread to the source terms of the incompressible fluid momentum equations through a spatial filtering operation, and the flow velocity around the Lagrangian droplets is corrected to account for their local flow disturbance. This allows accurate transport of Lagrangian droplets that are both smaller and larger than the fluid mesh spacing. The implementation of the algorithm for switching from and Eulerian toward Lagrangian framework is discussed, along with criteria validating a transformation. Then the Eulerian-Lagrangian coupling is applied to several test cases from the literature, and is compared to our in-house pure ICM solver on the atomization of a liquid jet. The results show that the Eulerian-Lagrangian coupling improves the physical analysis of the atomization, and achieves more accurate results for poorly resolved droplets.

Keywords: DNS, Two Phase Flow, Atomization, ICM, Eulerian-Lagrangian coupling

1. Introduction

Two phase flow atomization is involved in several natural and industrial applications, such as geyser eruption [1], jet sprinkler applications [2], liquid fuel injection in combustion chambers [3], and many others [4]. The analysis of atomization within a combustion chamber relies upon an accurate description of flow injection. Indeed, the injection and fragmentation of the jet create the initial conditions for the development of the spray, and therefore, allow for the estimation of important statistics such as total surface area. Thus, the scientific community has

*Corresponding author: jorge.brandle@coria.fr

put considerable efforts to describe liquid jet breakup, referred now as the primary atomization area [5]. This area involves complex phenomena such as turbulence, high momentum exchanges and break up events. Hence, robust experimental [6, 7], and numerical techniques [8–10], are required for a thorough understanding and description of the primary atomization area.

Direct numerical simulation (DNS) is an ideal tool to numerically investigate atomization. Interface capturing method (ICM) are often used to transport the interface between fluid and gas phases [11]. Several ICM have been successfully applied to analyze the primary atomization area, such as level set [12, 13], volume of fluid (VOF) [14, 15], or a coupling of both level set and VOF (CLSVOF) [16, 17]. With these methods, it is possible to accurately describe the liquid structure resulting from the breakup of the liquid jet, such as ligaments or large droplets. In particular, the CLSVOF method accurately represents the interface topology changes through the level set while taking advantage from the mass conservation properties of the VOF. In previous studies, our group applied the CLSVOF to several multiphase flows applications with complex interface topology change [18–20].

Ligaments and large droplets arising from primary breakup can experience successive breakups downstream to the jet [21]. Therefore, DNS must provide an accurate description of both the primary atomization and subsequent fragmentation, referred to as the secondary atomization [22]. Droplets in the secondary atomization area are several orders of magnitude smaller than the injected liquid jet. This leads to a significant scale range, from μm for droplets to mm for the liquid jet, that is too consequent to provide a complete description of a spray using current numerical resources. In addition to a poor physical representation of the secondary atomization, the transport of under-resolved droplets can generate numerical instabilities, known as *flotsam* or *jetsam*. Several solutions exist to circumvent this multiscale issue: to couple the fluid solver with an adaptive mesh refinement method [23], to model the transport of small fluid structures using a Lagrangian method [24], or, to simply remove these droplets from the DNS simulations [25]. Within the scope of this manuscript, small fluid structures are modeled.

This modeling approach, referred here to as the Eulerian-Lagrangian coupling [26, 27], combines the resolved transport of larger structures (ICM), and the modeling of under-resolved droplets (Lagrangian). A Lagrangian method is used to track these droplets, herein after called Lagrangian droplets. Semi-empirical correlations are used to transport Lagrangian droplets, relying upon instantaneous local fluid properties [28]. One of the challenges of this framework is to ensure a stable and conservative coupling at the transformation of an Eulerian droplet

toward a Lagrangian droplet, and vice-versa, without including artificial source terms to both frameworks. This goes with the definition of numerical and physical criteria of transformation and modification of the Eulerian fields.

In the pioneer works of Herrmann [26] and Tomar et al. [27], the Eulerian-Lagrangian framework is coupled with an adaptive mesh refinement (AMR). The Lagrangian framework is used to transport all Eulerian droplets far from the primary atomization. A two way Lagrangian coupling is used to transport Lagrangian droplets, accounting for both the transport of Lagrangian droplets and the fluid-droplets interphases momentum in the source terms of the fluid equations. After transformation, the fluid mesh is coarsened and the Lagrangian droplets are smaller than the fluid mesh. To distinguish between droplets, several criteria of transformation are used such as the distance between Eulerian droplets and other structures, or, the sphericity of Eulerian droplet. The latter enables transport of Lagrangian droplets using semi-empirical correlations derived from spherical shape [28]. The implementation of the Eulerian-Lagrangian coupling of Herrmann [26] and Tomar et al. [27] reduces the computational cost of the simulation while conserving an accurate description of the droplets' statistics downstream to the jet. However, results of Zuzio et al. [29] show that the coarsening of the fluid mesh during the transformation step can yield to numerical instabilities. They propose to first transport Eulerian droplet as a resolved solid particle, where all interactions between the fluid and the particle are resolved, ensuring a smooth transition toward coarser levels of the Eulerian fluid grid. This method requires adaptive mesh refinement which is challenging to implement.

In Ling et al. [30] an Eulerian-Lagrangian coupling for fixed Eulerian grid is proposed simplifying the Eulerian-Lagrangian coupling strategy. The transformation on a constant grid implies that Lagrangian droplets are larger than the fluid mesh spacing, yielding to a large local disturbance on the resolved flow. In the work of Ling et al. [30], this disturbance is filtered using a regularized weighted function to spread the coupling force over several droplets' diameter [31]. Despite the regularization of the Lagrangian droplets' feedback force, the local flow disturbance for Lagrangian droplets larger than the fluid mesh spacing are not filtered [32, 33]. This disturbance affects both the resolved flow and the Lagrangian droplets, as it yields to an inaccurate estimation of local fluid forces acting on Lagrangian droplets. Moreover, this flow disturbance is shown to be proportional to the number of cells across the diameter of the Lagrangian droplet, which deteriorates the accuracy of the Eulerian-Lagrangian coupling on a constant grid.

To circumvent large local disturbances on the resolved flow when dealing with particles

larger than the fluid mesh spacing, Evrard et al. [34] propose an Eulerian-Lagrangian coupling based on the filtering of the governing equations [35, 36]. It relies upon the filtering of the volume fraction, the drag force experienced by the particles, and the fluid velocity, as well as exchanges between the Eulerian and the Lagrangian frameworks. The results presented in the work of Evrard et al. [34] drastically improve the accuracy of the transport of the dispersed phase within the Lagrangian framework, however it requires the transport of the volume fraction as well as modification of the Poisson solver resolution.

Another solution to improve the Lagrangian transport of the particles larger than the fluid mesh spacing is to subtract the local flow disturbance by recovering the local undisturbed velocity through an analytical analysis of the Stokes and Oseen flow solutions [37, 38]. In Balachandar et al. [37] and Evrard et al. [38], the flow disturbance correction enables accurate transport of Lagrangian droplets larger than the fluid mesh. In addition, this method does not require the modification of the fluid solver. Thus, it is an ideal solution to transport the dispersed phase within the Lagrangian framework in the Eulerian-Lagrangian coupling. The fundamental originality of our study is the implementation, validation, and analysis of this coupling.

The present method couples a resolved transport of large fluid structures with the CLSVOF method of Ménard et al. [16] and a modeling of the small droplets with a Lagrangian two way coupling on the same grid level. A spatial filtering operation through a regularization of the force coupling is used [30], along with the correction of local flow disturbance derived in Evrard et al. [38] to transport Lagrangian droplets larger than the fluid mesh spacing. Although the implementation is straightforward because both Eulerian and Lagrangian solvers are independent, the analysis of the transformation step shows a mass inconsistency in the Lagrangian toward Eulerian transformation. A cost-efficient solution based on a minimization algorithm is proposed, reducing the error of several orders of magnitude. Additionally, all criteria of transformation implemented within this work are discussed along with their algorithms of implementation to provide a guideline for future implementations. The new method, as well as the new transformation criteria, are validated among reference cases from the literature, and successfully applied to two phase flow atomization of a liquid jet.

The manuscript is organized as follows. Section 2 presents the general framework, the interface capturing (ICM) and the Lagrangian particle tracking methods. In Section 3, limits of the ICM are investigated, as the basis of Eulerian-Lagrangian coupling. Section 4 presents the general Eulerian-Lagrangian coupling framework, and focuses on the criteria used to validate

both transformations. The Eulerian-Lagrangian coupling is thoroughly studied over a series of numerical examples in Section 5, validating the conservation of mass and momentum. In Section 6 the Eulerian-Lagrangian coupling is applied to the study of two phase flow atomization of a cross flow configuration, previously studied in the work of Herrmann [39]. Concluding remarks are outlined in Section 7.

2. Methodology

2.1. Eulerian framework

2.1.1. Interface Capturing Method

The transport of the interface is done by coupling the level set with the Volume of Fluid method (VOF), referred to as CLSVOF [40]. The motivation of this coupling is to benefit from both the second order geometrical accuracy of the level set and the mass conservative properties of the VOF. In this section, the methodology is briefly introduced, and the reader is referred to Ménard et al. [16] for a meticulous description of the CLSVOF and its implementation within our flow solver.

The location of the interface is defined from the signed level set distance function $\phi(\mathbf{x})$, where $\phi(\mathbf{x}) < 0$ indicates the gas fluid phase, $\phi(\mathbf{x}) > 0$ the liquid fluid phase, and $\phi(\mathbf{x}) = 0$ the interface. The volume occupied by the fluid phase (VOF), F, in a cell is obtained from the *VOFTools* library [41]. Then, the VOF and the level set, F and ϕ, are advected using a transport equation. For the level set field, it reads

$$\frac{\partial \phi}{\partial t} + \mathbf{u} \cdot \nabla \phi = 0\,, \tag{1}$$

whith $\mathbf{u}$ the fluid velocity vector. The VOF being a passive scalar, the same transport equation, Eq. 1 is used to advect F. Eq. 1 is solved with a second order conservative operator split advection scheme [40]. To conserve the numerical stability of our solver, a volume restriction algorithm is implemented that removes small numerical artifacts of VOF from the computational domain. It reads for the kth fluid cell as

$$F_k = \begin{cases} 0 & \text{if } F_k < \epsilon_F \quad \text{or} \quad \text{No interface in all neighbor cells} \\ 1 & \text{if } F_k > 1 - \epsilon_F \quad \text{or} \quad \text{No interface in all neighbor cells} \\ F_k & \text{otherwise} \end{cases} \tag{2}$$

where ϵ_F is the numerical threshold for the VOF quantity, set to $\epsilon_F = 1 \times 10^{-12}$ and ϵ_ϕ the numerical threshold for the level set distance, set to $\epsilon_\phi = \frac{3}{4}\sqrt{3}\Delta x$, with Δx the mesh spacing. Each time step, the position of the level set at the interface is corrected from the VOF updated field, ensuring conservation of geometric properties and mass. To preserve the sign distance properties of the level set function, a redistancing algorithm is applied at the end of each time step

$$\frac{\partial d}{\partial \tau} = \text{sign}(\phi^n)\left(1 - |\nabla d|\right), \quad \text{where } d(\mathbf{x}, \tau)_{\tau=0} = \phi^n(\mathbf{x}, t) \tag{3}$$

where τ is a fictitious time, and d is used to ensure the distance property. After solving Eq. 3, the level set field is updated, setting $\phi^{n+1} = d$. Finally, the classical projection method is applied, updating the velocity and the pressure fields (Section 2.1.2).

2.1.2. Projection method

The fluid phase is considered an incompressible Newtonian fluid subject to the Navier-Stokes equations and reads as

$$\nabla \cdot \mathbf{u} = 0\,, \tag{4}$$

$$\rho \frac{\partial \mathbf{u}}{\partial t} + \nabla \cdot (\rho \mathbf{u} \otimes \mathbf{u}) = -\nabla P + \nabla \cdot \mathcal{D} + \mathbf{f}\,, \tag{5}$$

where ρ is the density, P the pressure, $\mathcal{D}$ the strain rate tensor, and $\mathbf{f}$, a volume force accounting for the presence of particles, surface tension force, and external forces such as gravity $\mathbf{g}$. The strain rate tensor is defined as

$$\mathcal{D} = \mu\left(\nabla \mathbf{u} + (\nabla \mathbf{u})^T\right)\,, \tag{6}$$

with μ the dynamic viscosity.

A standard projection method is used to solve the system after the interface transport. The first step is to solve the momentum equation excluding the pressure terms at the current time step n. This predictor step reads

$$\mathbf{u}^* = \mathbf{u}^n + \Delta t \left(- \left(\mathbf{u}^n \cdot \nabla \right) \mathbf{u}^n + \frac{1}{\rho^{n+1}} \left(\nabla \cdot \mathcal{D} + \mathbf{f}^n \right) \right) , \tag{7}$$

where Δt is the nth time step. The pressure is obtained from the intermediate velocity field $\mathbf{u}^*$ as a solution of an implicit system (Poisson equation)

$$\nabla \cdot \left(\frac{1}{\rho^{n+1}} \left(\nabla P^{n+1} \right) \right) = \nabla \cdot \mathbf{u}^*. \tag{8}$$

Finally, the velocity at the next time step is obtained as

$$\mathbf{u}^{n+1} = \mathbf{u}^* + \frac{1}{\rho^{n+1}} \left(-\nabla P^{n+1} \right) . \tag{9}$$

The momentum flux computation is discretized with a fifth-order WENO scheme in a conservative form [18]. The viscous term is discretized with the algorithm of Sussman and Puckett [40]. The pressure, density and viscous jumps across the interface are handled using a ghost fluid method, that consists of extrapolating fluid quantities on both sides of the interface, preventing discontinuities in the derivation of fluid variables for a sharp interface method [42]. The Poisson equation is solved with a Conjugate Gradient preconditioned by a Multi-grid Method coupled with a Red-Black Gauss-Seidel algorithm [43]

2.1.3. Time integration

The temporal integration is done with a second order TVD Runge-Kutta explicit time scheme. An adaptive time stepping is used based on the convection, viscosity, surface tension and gravity. The adaptive time step, Δt, is estimated from these constraints as in Kang et al. [42]. In the present work, the CFL condition is fixed to $K_{CFL} = 0.3$ to ensure the stability of the approach.

2.2. Lagrangian framework

To circumvent the shortcomings of the ICM, under-resolved droplets are modeled with a Lagrangian tracking method (Section 2.2.1), and the droplets' momentum is transferred toward the source terms of the fluid momentum equation (Section 2.2.2). A flow disturbance correction is coupled with a spatial filtering of the feedback force to prevent over estimation of hydrodynamic forces experienced by Lagrangian droplets (Section 2.2.3).

2.2.1. Lagrangian transport

The motion of a rigid Lagrangian droplet obeys Newton's second law

$$\frac{d\mathbf{X}_p}{dt} = \mathbf{U}_p \,, \tag{10}$$

$$m_p \frac{d\mathbf{U}_p}{dt} = \sum \mathbf{F}_p \,, \tag{11}$$

where m_p, $\mathbf{X}_p$, $\mathbf{U}_p$, and $\mathbf{F}_p$ are the mass, coordinates, velocity, and sum of the forces acting on a Lagrangian droplet. The resultant of forces reads

$$\mathbf{F}_p = \mathbf{F}_{p,ext} + \mathbf{F}_{p,fluid} \,, \tag{12}$$

with $\mathbf{F}_{p,ext}$ accounting for the action of external forces on Lagrangian droplets, reduced to the gravitational acceleration in this work, and $\mathbf{F}_{p,fluid}$ the action of the fluid which reads

$$\mathbf{F}_{p,fluid} = \frac{3}{4} \frac{\rho_f V_p C_D}{D_p} |\mathbf{U}_{slip}| \mathbf{U}_{slip} \,, \tag{13}$$

where V_p and D_p are the volume and diameter of the Lagrangian droplet, $\mathbf{U}_{slip}$ is the difference between the velocity of the Lagrangian droplet, $\mathbf{U}_p$, and the velocity of the fluid phase interpolated at the position of the droplet, $\mathbf{u}_{f@p}$. The coefficient C_D is a drag coefficient obtained from the correlation of Schiller and Naumann [44] and varies with respect to the Lagrangian droplet's Reynolds number

$$Re_p = \frac{\rho_f D_p |\mathbf{U}_{slip}|}{\mu_f}. \tag{14}$$

2.2.2. Momentum coupling

The feedback force accounting for the presence of the droplets is transferred toward the fluid with a smooth regularized kernel function [31]. A Gaussian kernel is used

$$G(\mathbf{x}) = (2\pi\sigma)^{-2/3} e^{\frac{-|\mathbf{x}|^2}{2\sigma^2}}, \tag{15}$$

where σ is the length controlling the region of the force spreading. Ideally, the support of the Gaussian kernel is of infinite length, but, for computational efficiency the support is considered of finite length, referred to as compact support. This assumption is valid because the Lagrangian droplet mostly affects its local surrounding. The main drawback of a compact support with a Gaussian kernel is that the momentum transfer is not fully conservative, however by adequately choosing σ we can ensure that at least 99% of the energy is transferred over this compact support. The volume force $\mathbf{f}_p$ in Eq. 5 reads

$$\mathbf{f}_p = \sum_{i=1}^{Np} = \mathbf{F}_{p,i} G(|\mathbf{x} - \mathbf{X}_{p,i}|). \tag{16}$$

The analytical discretization of the Gaussian filter for a Cartesian uniform grid is used [38]. It reads for an arbitrary 2D cell $k_{i,j}$

$$G(\mathbf{X}_p) = \frac{1}{V_K} \int_{V_K} G(|\mathbf{x} - \mathbf{X}_p|) d\mathbf{x} = \frac{\left[\mathrm{erf}\left(\frac{x - X_p}{\sigma\sqrt{2}}\right)\right]_{x_i}^{x_{i+1}} \left[\mathrm{erf}\left(\frac{y - Y_p}{\sigma\sqrt{2}}\right)\right]_{y_j}^{y_{j+1}}}{4(x_{i+1} - x_i)(y_{j+1} - y_j)}, \tag{17}$$

where $V_k = [x_i, x_{i+1}] \times [y_j, y_{j+1}]$ is the discretized volume of the cell k.

2.2.3. Velocity disturbance correction

The velocity interpolation at the position of the Lagrangian droplet, $\mathbf{u}_{f@p}$, can be decomposed between two contributions as

$$\mathbf{u}_{f@p} = \tilde{\mathbf{u}}_{f@p} + \mathbf{u}^{'}_{f@p}\,, \tag{18}$$

where $\mathbf{u}^{'}_{f@p}$ is the estimation of velocity disturbance arising from the momentum coupling at the position of the droplet, and, $\tilde{\mathbf{u}}_{f@p}$ is the reconstruction of the interpolated velocity, $\mathbf{u}_{f@p}$, filtering the velocity disturbance.

An analytical correction to the flow disturbance in Eq. 18 is derived for the Stokes flow through the regularized momentum contribution of the Lagrangian droplet, and, extended to finite Reynolds number accounting for the Oseen's approximation of the Navier-Stokes equations [37, 38]. In the respective works of Balachandar et al. [37] and Evrard et al. [38], a point-wise correction and an averaged velocity correction based are derived, respectively. Both methods have been coupled and tested within our flow solver, the averaged correction is conserved for numerical stability reasons. This correction reads as

$$\tilde{\mathbf{u}}_{f@p} = A(\mathbf{u}_{f@p})_{\lambda} - \frac{\mathbf{f}_p \psi_{St}(\lambda/\delta)\psi_{Os}(Re_G)}{2\pi\mu_f \delta}\,, \tag{19}$$

where δ is the compact support of integration for a Wendland kernel, linked to the Gaussian kernel by

$$\delta = \frac{\sigma}{\sqrt{2/9\pi}}\,, \tag{20}$$

used as controlling length in Eq. 17. λ is the size of the averaging regularized support and is chosen as

$$\lambda = \max(\delta, 2\Delta x)\,, \tag{21}$$

and the averaged velocity over the length λ, $A(\mathbf{u}_{f@p})_{\lambda}$ obtained through the convolution of the velocity through the regularized kernel function defined in Eq. 15,

$$A(\mathbf{u}_{f@p})_\lambda = \frac{1}{V_\Omega}\int_\Omega G(|\mathbf{x}-\mathbf{X}_p|)\mathbf{u}(\mathbf{x})d\mathbf{x}, \tag{22}$$

with Ω the domain of convolution of the regularized kernel function and V_Ω its equivalent volume. The corrections ψ_{St} and ψ_{Os} are the Stokes and Oseen corrections given in Appendix A.

2.2.4. Time integration

The Lagrangian quantities are temporally integrated with a second order Runge-Kutta temporal schemes. The coupling between Lagrangian and Eulerian frameworks is split, which gives more flexibility for both implementations. The coupling follows the steps listed in algorithm 1 for a first order time scheme, where Capital letters indicate Lagrangian quantities.

Algorithm 1: Lagrangian solver coupling with flow solver

foreach *Lagrangian droplet* **do**
- Interpolate $\mathbf{u}_{f@p}$ from $\mathbf{u}^n$
- Apply flow disturbance corrections (Section 2.2.3)
- Compute fluid forces $\mathbf{F}_p^n$
- Transport Lagrangian droplets ($\mathbf{U}_p^{n+1}$, $\mathbf{X}_p^{n+1}$, Section 2.2.1)
- Regularize $\mathbf{F}_p^n$ and add to source terms $\mathbf{f}^n$ (Section 2.2.2)

end

Add $\mathbf{f}^n$ to predictor step (Eq. 7).

3. Analysis of the numerical limits of the ICM

In this section, we study the limits of the ICM methods in the simulation of under-resolved droplets on a classical test case, a sedimented droplet falling in a box [29, 30, 34]. The configuration is also used to validate the implementation of the Lagrangian framework (Section 2.2).

3.1. Numerical configuration

We analyze the temporal evolution of a sedimented spherical droplet falling in a box under gravity. The computational domain is a rectangular box of size $Lx \times Ly \times Lz$ with $Lx = Lz = Ly/2$ and $Lx = 1\times10^{-3}\ m$. Wall boundary conditions are used everywhere but the top face along y which is set to a outflow boundary condition. The physical properties are taken from Ling et al. [30], $D_p/Lx = 0.1$, with D_p the diameter of the Lagrangian droplet, $\rho^* = \rho_l/\rho_g = 100$, with ρ_l and ρ_g the density of the liquid and the gas, respectively, and $\mu^* = \mu_l/\mu_g = 10$, the viscous ratio, only relevant to the Eulerian droplet. Surface tension forces are not considered in

the Eulerian droplet [29]. The gravitational acceleration is set to $\mathbf{g} = 9.81\ m/s^2$. The terminal velocity of the droplet is obtained by balancing gravity and drag forces (Eq. 13). To account for the confined environment, the terminal velocity of the droplet is multiplied by a semi-empirical parameter modeling the confined environment [45], giving

$$V_{\tau_p} k_\eta = 4.112 \times 10^{-2}\ \mathrm{m/s}\,, \tag{23}$$

with k_η set to $k_\eta = 0.824$ for this configuration.This set of parameters gives a particles' Reynolds number of $Re_p = 0.4112$.

The Eulerian droplet can be compared to the Lagrangian droplet only if it remains spherical. Subsequent snapshots of the interface of the Eulerian droplet falling in the box are presented in figure 1. The results show that these physical parameters almost maintain the spherical shape of the Eulerian droplet, allowing the comparison of both methods.

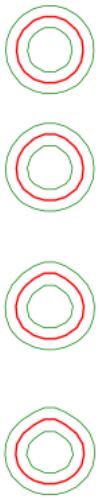

Figure 1: Successive representations of the interface of the sedimented Eulerian droplet falling within a box. Interface is shown at distances $\phi(x) = [-\Delta x; 0; \Delta x]$, in green, red, green, respectively. Results are obtained at $D_D/\Delta x = 6.4$ at $t/\tau_p = [0, 1.8, 3.6, 4.5]$, from top to bottom.

Since we are interested in the performance of ICM method in the coarse regime, we vary the numerical resolution of ICM simulation in the range $D_D/\Delta x = 3.2, 4.8, 6.4, 8$ and 16, with D_D the diameter of the droplet. Simulations with finer resolution are used to compute a reference solution for the ICM method. Simulations below the numerical resolution $D_D/\Delta x = 3.2$ are unstable. On the other hand, the two way method employed in the present Eulerian-Lagrangian coupling is also tested. Thus, the two way approach simulations vary over the range $D_p/\Delta x = 0.4, 0.8, 1.6, 3.2$ and 4.8. This corresponds to the numerical resolution where the resolved ICM

cannot accurately transport the droplets. The size of the regularized kernel support affects the drag force experienced by the Lagrangian droplet. Therefore, we vary the length of the Gaussian regularized kernel support, δ, over several Lagrangian droplets' radii (R_p) $\delta = 3R_p, 5R_p, 7R_p$ and $10R_p$, where the upper bounds are given by the size of the box. The two way coupling results without flow disturbance corrections are obtained with the method presented in Ling et al. [30] to transport the small droplets in the Eulerian-Lagrangian coupling. The averaging kernel length varies accordingly to δ (Eq. 21).

3.2. Results

3.2.1. Lagrangian solver

The temporal evolution of the Lagrangian droplets' velocity scaled by the terminal velocity, Eq. 23, is presented in figure 2. The simulation time is scaled by the particles' characteristic time $\tau_p = \frac{\rho_p D_p^2}{18\mu_f}$.This figure is organized as follows, the columns present the results with the self-disturbance correction (left), and without (right). In the latter, a trilinear interpolation is used to obtain $\mathbf{u}_{f@p}$. The four rows show the evolution of length of the Gaussian regularized kernel support δ (increases from top to bottom). The color map indicates the numerical resolution, and, the solid black line shows the results for the equivalent one way coupling. The one way results are used as a numerical reference solution because flow disturbance is null, $\mathbf{u}^{'}_{f@p} = 0$.

For both two way approaches, the number of fluid cells across the diameter of the particle affects the temporal evolution of the particle and its terminal velocity. We observe an overestimation of the terminal velocity proportional to the number of fluid cells across the diameter, the worst results are obtained at $D_p/\Delta x = 4.8$. These observations agree with the literature [37, 38].

The results with the self-disturbance correction reduces the influence of the flow disturbance in the two way coupling. For example, at $\delta = 3R_p$ and $D_p/\Delta x = 4.8$, the correction prevents the solver from diverging (the results without correction are numerically unstable). Yet, at $\delta = 3R_p$ and $D_p/\Delta x = 4.8$ the terminal velocity is overestimated by a factor 1.5. To increase accuracy at high $D_p/\Delta x$ the size of the spatial filter, δ, can be increased. For example at $\delta = 10R_p$, the reference results are recovered. Nonetheless, the larger is the support of the regularized function, the more expensive is the two way coupling, i.e. integration of the flow variable and spreading of the particles' momentum on a larger compact support. Therefore, the choice of δ results from a trade-off between physical accuracy and computational cost.

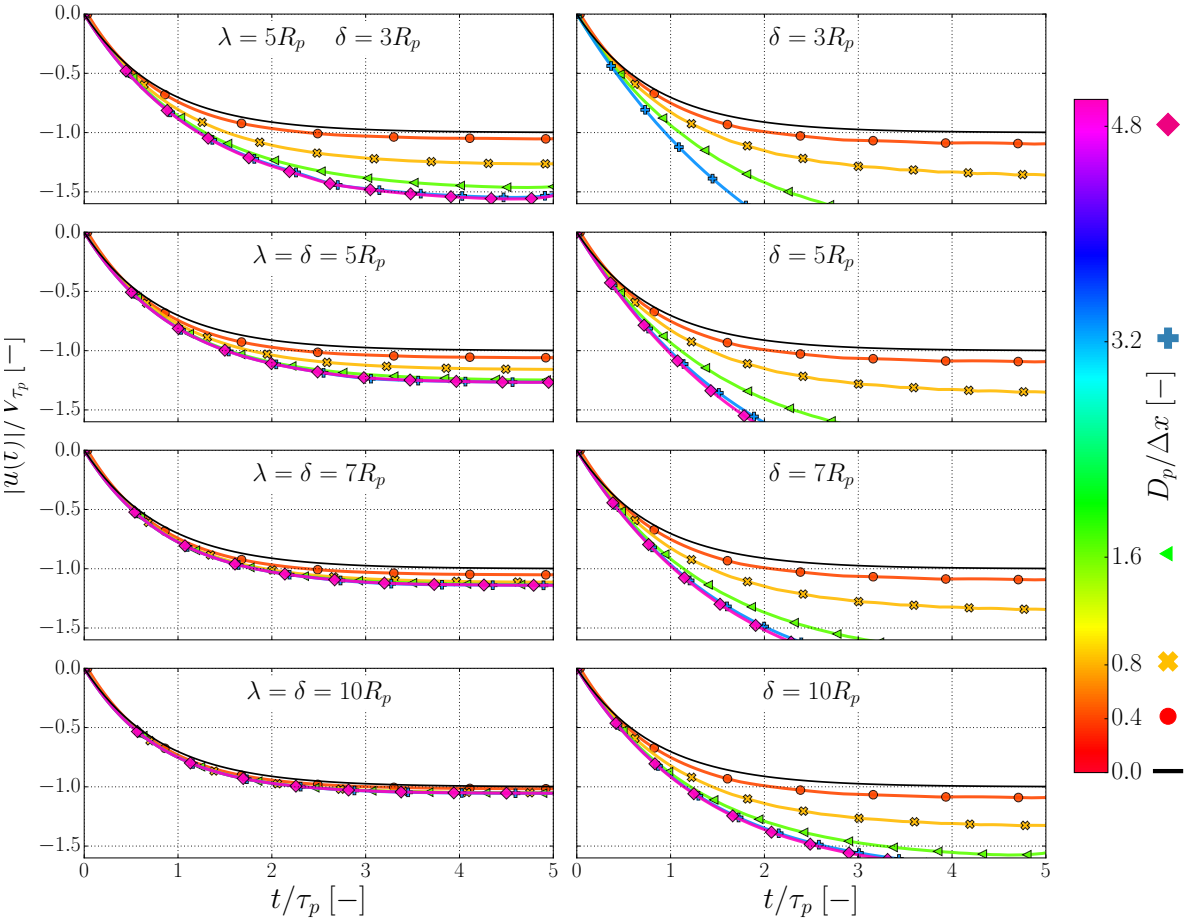

Figure 2: Temporal velocity evolution of the sedimented free-falling particle scaled by the terminal velocity V_{τ_p} using the two way Lagrangian coupling. Left column: two way coupling including self-disturbance corrections on the averaged velocity interpolation Eq. 19. Right column: without corrections using a trilinear interpolation. Results are obtained for four support size, $\delta = [3R_p; 5R_p; 7R_p; 10R_p]$ (from top to bottom) and numerical resolutions $D_p/\Delta x = [0.4; 0.8; 1.6; 3.2; 4.8]$ (color map and symbols). Black solid line shows the one way coupling evolution.

3.2.2. Eulerian solver

The ICM results are shown in the figure 3a. The ICM results converge at a terminal velocity higher than the reference one. This is because the reference terminal velocity is given for a solid spherical particle and the ICM resolves two-phase flow.

A new reference velocity is computed for these results using a Richardson extrapolation from the results obtained at $D_D/\Delta x = 6.4, 8$ and 16. This value is $V_R = 4.55 \times 10^{-2}$ m/s. At low resolution, the reference terminal velocity of the droplet is underestimated by the coarse numerical resolution. For example, at $D_D/\Delta x = 3.2$, we observe an underestimation of 26.3% of the terminal velocity. For numerical resolutions higher than $4.8 D_D/\Delta x$ the error drops below 10%, and the ICM method recovers the reference results under spatial refinement.

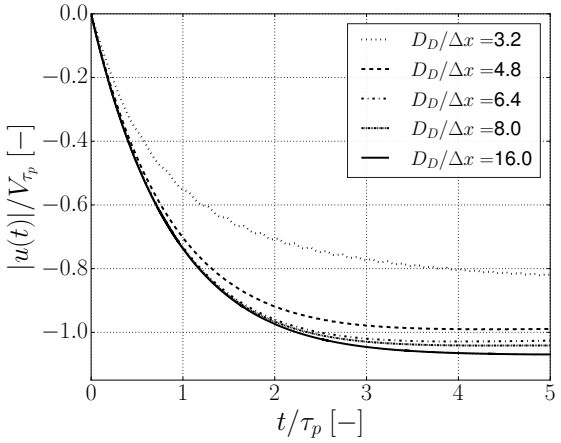

(a) Temporal evolution of the Eulerian droplet (ICM) velocity against characteristic time for several numerical resolutions.

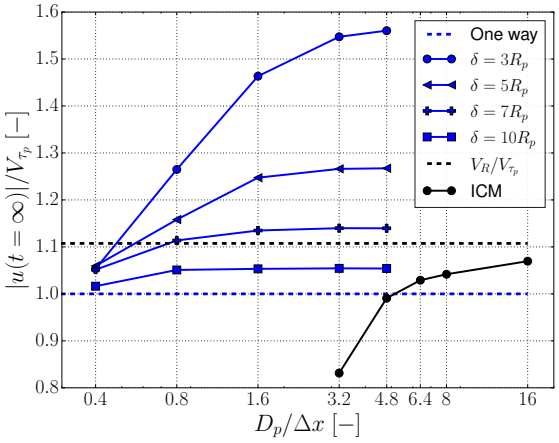

(b) Spatial convergence of the terminal velocity for the Eulerian droplet and two way Lagrangian coupling with self-disturbance correction varying the support size δ. Reference: dashed line.

Figure 3

3.2.3. Numerical limits

The snapshots of the velocity fields are extracted at the same time step for the three studied configuration, at $D_p/\Delta x = 4.8$, and are reported in figure 4. The main differences are the location of the droplet at the same time step and the local velocity field in the surrounding of the droplets. The fluid velocity reaches a higher magnitude with the ICM method, meanwhile it is significantly lower with the two way coupling without corrections. These differences do not alter the main velocity pattern: the recirculation in-between the droplet and the walls is observed for all cases. The location of the droplets agrees with the temporal evolution of the velocity of the droplets, see figure 2 and left figure 3b; this shows the importance of the velocity disturbance correction in the two way coupling.

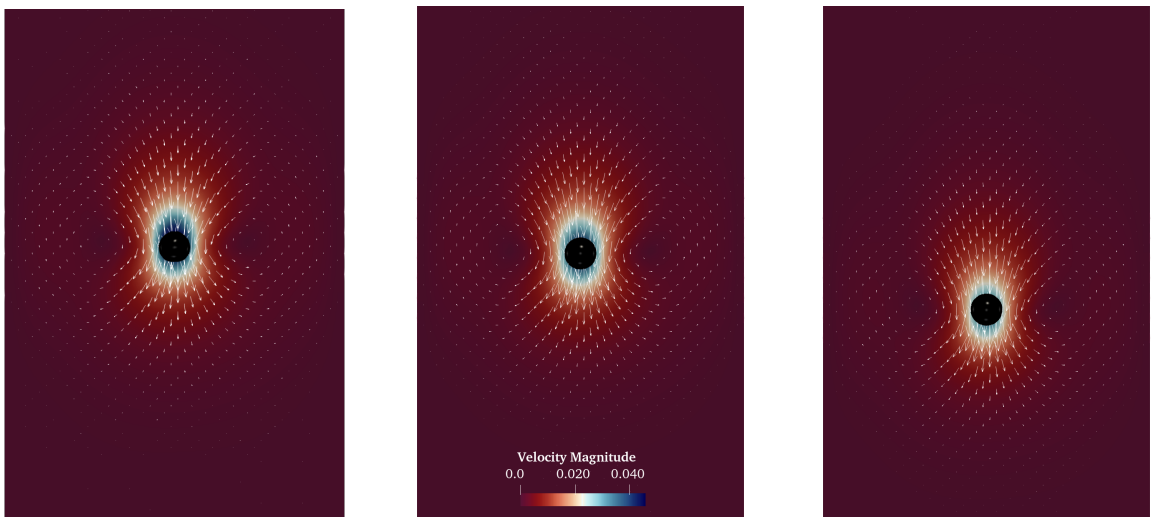

Figure 4: Velocity field around the free-falling sedimented droplet at $D_p/\Delta x = 4.8$ at time $t/\tau_p = 1.8$. Left: CLSVOF, Center: two way Lagrangian method with correction, Right: two way Lagrangian method without correction (filter length $\delta = 7R_p$).

The terminal velocity obtained with the ICM and the two way Lagrangian coupling, including the self-disturbance corrections, are compared for the entire spectra of numerical resolutions. The terminal velocity is scaled by the reference velocity V_{τ_p}, and the results are shown in figure 3b. The reference velocity of the ICM method obtained from the Richardson extrapolation of our results is also reported. Above 4.8 fluid cells across the diameter, the ICM accurately transports the droplets and the results are close to the Richardson's reference velocity. For $D_p/\Delta x = 4.8$, only the two way results obtained with the length $\delta = 10R_p$ improves the results of ICM method. At $D_p/\Delta x = 3.2$, the necessary filter width to improve the ICM method is of $\delta = 7R_p$. In addition, the results below $\delta = 7R_p$ do not improve the transport of the droplets in the range $D_p/\Delta x \geq 3.2$. Therefore, the filter length δ is always set to $\delta = 7R_p$ if not stated otherwise in the manuscript.

4. Eulerian-Lagrangian coupling

4.1. From the Eulerian droplet toward the Lagrangian particle

This section discusses the steps, from the selection of criteria of transformation toward the reconstruction of the Eulerian fields after transformation, required to switch from Eulerian framework toward the Lagrangian one, and vice-versa. The first step consists in the detection of all Eulerian and Lagrangian droplets in the computational domain.

While the knowledge of the Lagrangian droplets' coordinates is natural in the Lagrangian framework, this is not straightforward for the ICM. A labeling algorithm is used to identify all

the fluid structures by associating a group of neighboring fluid cells [26, 27], that can represent the liquid core of an atomized jet, a ligament, a droplet, etc.

From this algorithm can be derived Lagrangian statistics, such as the volume of the droplet, used to define a numerical resolution criterion, the distance to other structures, or to qualify the droplet as spherical under a morphological analysis. These steps are summarized in algorithm 2.

Algorithm 2: Eulerian-Lagrangian coupling: Eulerian droplet transformation.

```
Get labeling field (Section 4.1.1)
foreach Labelled structure j do
    Compute structure volume V_j and equivalent diameter D_{eq,j} (Section 4.1.1)
    if Droplet under resolved then
        Compute distance to other fluid structures L_D (Section 4.1.3)
        if Droplet isolated then
            Compute morphological parameters α_j and ι_j (Section 4.1.4)
            if Droplet is spherical then
                Add j to the droplets' transformation list
            end
        end
    end
end
foreach Droplet in transformation list do
    Update VOF and level set fields (Section 4.1.5)
    Update Velocity field (Section 4.1.6)
    Remove Eulerian droplet and add it to Lagrangian droplet list
end
```

4.1.1. Detection of fluid structures

General algorithm

The implementation of the labeling algorithm combines both the VOF and level set fields, and is applied for the kth cell as

$$\mathcal{X}_k = \begin{cases} i_k & \text{if } F_k \geq \epsilon_F \text{ and } \phi_k \geq -\epsilon_\phi \\ 0 & \text{otherwise} \end{cases} \tag{24}$$

where $\mathcal{X}$ is the label field, i is the value associated to the kth fluid cell, and ϵ_F and ϵ_ϕ are thresholds based on the desired accuracy. Here ϵ_F is set to 10×10^{-10} and ϵ_ϕ to $\sqrt{\frac{3}{4}\Delta x^2}$ (being the distance from the edge of a cube to its center). The level set is used to filter small VOF artifacts. From the labelled field a linked list connects all labelled fluid cells with a value strictly superior to 0 to its neighbors. Following the required MPI communications, all the labelled

belonging to the fluid cells in a fluid structure are switched to the smallest value to provide a unique label to each droplet.

Figure 5 shows the three steps of the algorithm, 1) identification of the fluid structures based on the VOF and level set fields, 2) labeling of all the fluid cells $\mathcal{X}$, 3) fix the label of all fluid cells in the same fluid structure to the minimum value after MPI communications. The last step illustrates the configuration where a small droplet, $\mathcal{X} = 3$, is grouped with a neighboring structure because of the poor numerical resolution.

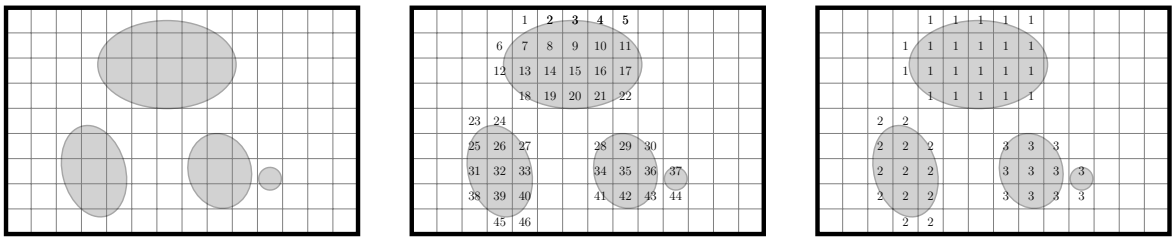

(a) Droplets shown in gray, level set iso-contour at $\phi = 0$.

(b) labeling of all fluid cells.

(c) Unique label per droplet.

Figure 5: Labeling algorithm.

Eulerian droplets tracking

The label field $\mathcal{X}$ is used to track Eulerian droplets coordinates, and to detect coalescence and break up events. The volume-based centroid of the droplets is obtained as

$$\mathbf{X}_j = \sum_{k=1}^{N_{cells}} F_k \mathbf{x}_k \delta_{k,j} \,, \tag{25}$$

with $\mathbf{X}_j$ the center of the jth fluid structure, F_k, $\mathbf{x}_k$ and $\mathcal{X}_k$ being the volume fraction, the center and the label of the kth fluid cell, respectively. $\delta_{k,j}$ is the Kronecker-Delta set to $\delta_{k,j} = 1$ if $k = j$ and 0 if $k \neq j$.

To track the spatial evolution of these structures, the Euclidean distance between the center of the jth fluid structure at time step n and the ith structures at the previous time step is computed. To reduce uncertainties a first order temporal integration scheme is used to advect the center of all the ith fluid structures at the previous time step $(n-1)$, and the comparison reads

$$|\mathbf{X}_j^n - \mathbf{X}_i^{n-1} + \Delta t \mathbf{V}_i^{n-1}| < \eta \Delta x \,, \tag{26}$$

with η a constant adapting to the calling frequency. This constant is set to $\eta = 1/2$ when the algorithm is employed at every time step.

In addition to the center-to-center distance computation, the volume variation is computed between two paired structures to ensure an accurate tracking. For the jth structure, the volume is obtained with

$$V_j = \sum_{k=1}^{N_{cells}} F_k \Delta x^3 \delta_{k,j} \tag{27}$$

An unpaired structure often results from a breakup or a coalescence event. To enhance the statistics, two algorithms are implemented to detect these events, and are given in Appendix B and Appendix C.

4.1.2. Numerical resolution criterion

A numerical resolution criterion, based on the fluid mesh spacing and the numerical size of the droplet, is defined. The volume-based-equivalent diameter of the studied droplet is used to compute the numerical size of the droplet. It is obtained from the volume of the jth fluid structure (see Eq. 27)

$$D_{eq} = 2\left(\frac{3}{4\pi} V_j\right)^{1/3}, \tag{28}$$

used to discriminate under resolved droplets,

$$D_{eq}/\Delta x \leq \epsilon_V,$$

with ϵ_V a numerical-resolution-based accuracy threshold.

Based on the analysis of the limits of the present ICM method in the simulation of under-resolved droplets, see Section 3, the value of ϵ_V is set to $\epsilon_V = 4$ if not stated otherwise in the manuscript.

4.1.3. Distance criterion $\mathcal{L}_D$

The distance criterion, $\mathcal{L}_D$, ensures that the Eulerian droplet is isolated before an eventual transformation. This prevents topology changes for the surrounding droplets resulting from the modification of the Eulerian fields, discussed in the Sections 4.1.5 and 4.1.6. From numerical experiment, the minimum distance $\mathcal{L}_D$ must satisfy

$$\mathcal{L}_D \geq D_{eq}\,, \tag{29}$$

to consider the Eulerian droplet isolated. This value prevents topology changes at the transformation from Eulerian droplet toward Lagrangian droplet.

The inequality in Eq. 29 consists of looping over the fluid cells near the droplet to detect any other fluid structure. The distance criterion is validated for the jth structure if all the fluid cells in a box given by

$$|x_{x,k}-(X_{x,j}+D_{eq,j}/2)\,| \leq D_{eq,j}\,, \quad |x_{y,k}-(X_{y,j}+D_{eq,j}/2)\,| \leq D_{eq,j}\,, \quad |x_{z,k}-(X_{z,j}+D_{eq,j}/2)\,| \leq D_{eq,j}\,,$$

have a label equal to zero or to the structure label. In the previous equation, $\mathbf{X}_j$ is the center of mass of the jth structure and $\mathbf{x}_k$ the center of the Eulerian grid.

4.1.4. Morphological criterion

Parameters definition

The morphological analysis of a fluid structure in 2D has been widely analyzed, see the detailed literature review of existing parameters of Ghaemi et al. [46]. On the other hand, few parameters exist to characterize fluid structures in 3D, such as the eccentricity parameter defined in Herrmann [26] who scales the maximal distance to the interface from the center of the droplet by the volume-based-equivalent radius of the droplet, or the sphericity parameter defined in Zuzio et al. [29], Arienti et al. [47] who scales the minimum distance to the interface from the center of the droplet by the volume-based-equivalent radius of the droplet. In a previous work [48], our research group analyzed 3D morphological parameters, and showed that the aspect ratio [49], and the irregularity [50], are relevant morphological parameters to study the shape of a 3D droplet. The aspect ratio, α, reads

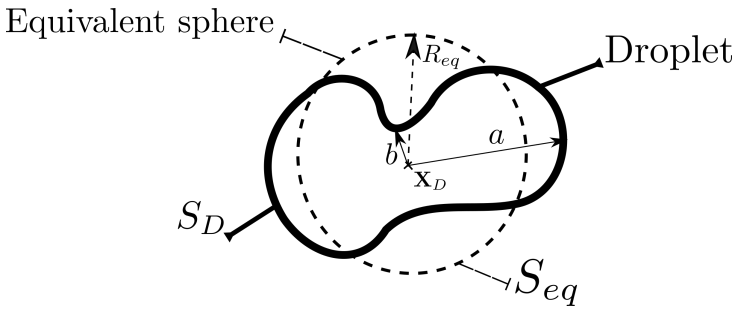

Figure 6: Construction of the aspect ratio α and irregularity ι from the lengths a, b and quantities of surface S_D, $S_{eq} = 4\pi R_{eq}^2$, for a peanut like droplet.

$$\alpha = \frac{b}{a}\,, \tag{30}$$

with a and b the maximum and minimum distances from the center of mass of the droplet to its interface. The irregularity ι reads

$$\iota = \frac{S_{\mathcal{S}}}{S_{\mathcal{D}}}\,, \tag{31}$$

with $S_{\mathcal{S}}$ the surface of the volume-based-equivalent sphere of radius R_{eq}, see Eq. 28, and $S_{\mathcal{D}}$ the surface of the droplet. The computation of the quantities a, b, S_D for a droplet and R_{eq} for the equivalent sphere is schemed in figure 6. These two parameters are bounded over $[0; 1]$ with 1 for a perfect sphere and 0 for an infinite cylinder.

Parameter thresholds

The goal of this numerical test case is to provide a value for the parameter thresholds based on the irregularity and the aspect ratio. The Eulerian droplets candidate to transformation are under-resolved, see Section 4.1.2; Chéron et al. [48] show that it results in an overestimation of the deformation of the droplets. Thus, the numerical accuracy of the aspect ratio and irregularity is studied for realistic droplets in a spray by extending the spatial convergence analysis of Chéron et al. [48] to spheroidal shapes. The results of this numerical test case is used to provide a value for the parameters thresholds based on the irregularity and the aspect ratio, ϵ_ι and ϵ_α, respectively.

In this numerical test, the spheroid is created using an analytical equation, and is centered in a cubic domain of size $4D_{eq}$. The morphological parameters are directly computed without

solving the fluid equations. For coarse resolution, the location of the centroid of the spheroid affects the estimation of the morphological parameters, creating a mesh dependency. Thus, several simulations are performed varying the location of the centroid of the spheroid, and averaged, maximum and minimum values are reported.

The initial shape of the spheroids is based on the aspect ratio and varies in the range $\alpha = 0.5$ to 1 with an increment of 0.05. The numerical resolution of the spheroids varies in the range $D_{eq}/\Delta x = 2$ to 36, with a volume

$$V_D = \frac{4}{3}\pi a b^2 \quad \text{with } a \geq b. \tag{32}$$

The averaged, maximum and minimum values are reported in figure 7a for the aspect ratio, α, and in figure 7b for the irregularity, ι (for clarity not all the results are shown). The two parameters converge toward their expected values for well resolved interfaces, regardless of the initial deformation of the spheroid. At coarse resolution, the mean of both parameters always underestimate the expected value, thus over-estimating the deformation of the droplets. For the aspect ratio, the more flattened is the spheroid the higher is the overestimation. For instance, at $\alpha = 0.5$, 10 fluid cells across the diameter are required to reach an error of 1%, meanwhile accurate results are obtained with 4 fluid cells across the equivalent diameter when $\alpha \geq 0.85$. The same variation is observed for the extreme values. In opposition to the aspect ratio, the spatial convergence of the mean, minimum, and maximum irregularity parameter does not show a dependence to the shape. For example at $D_{eq}/\Delta x = 4$, a mean error below 10% is reached for all spheroids.

The average values of aspect ratio and irregularity show an over-estimation of the deformations of the droplets in the coarse regime. To circumvent the over-estimation of the shape deformation, the criteria of transformations based on the morphological parameters α and ι must allow 'non-spherical' droplets to be transformed. To do so, their values are set to $\epsilon_\alpha = 0.65$ for the aspect ratio based threshold, and $\epsilon_\iota = 0.85$ for the irregularity based threshold.

4.1.5. Eulerian transformation: reconstruction of the level set and VOF

At the transformation from Eulerian droplet toward Lagrangian droplet, the level set and VOF fields represent an Eulerian droplet that no longer exist in the Eulerian framework. In the literature, the methodologies to reconstruct the VOF and level set fields vary. In our flow

solver, the VOF field is updated setting

$$F_k = \begin{cases} 0 & \text{if } \mathcal{X}_k = \mathcal{X}_j \\ F_k & \text{otherwise,} \end{cases} \tag{33}$$

and the level set, setting

$$\phi(\mathbf{x})^{rec} = \min\left(\phi(\mathbf{x}), \sqrt{|\mathbf{x}_D - \mathbf{x}|^2} - 6D_{eq}\right) , \tag{34}$$

over the entire computational domain to conserve the continuous description of the level set. In Eq. 34 the negative signed distance ensures that the fluid phase is removed (in our solver

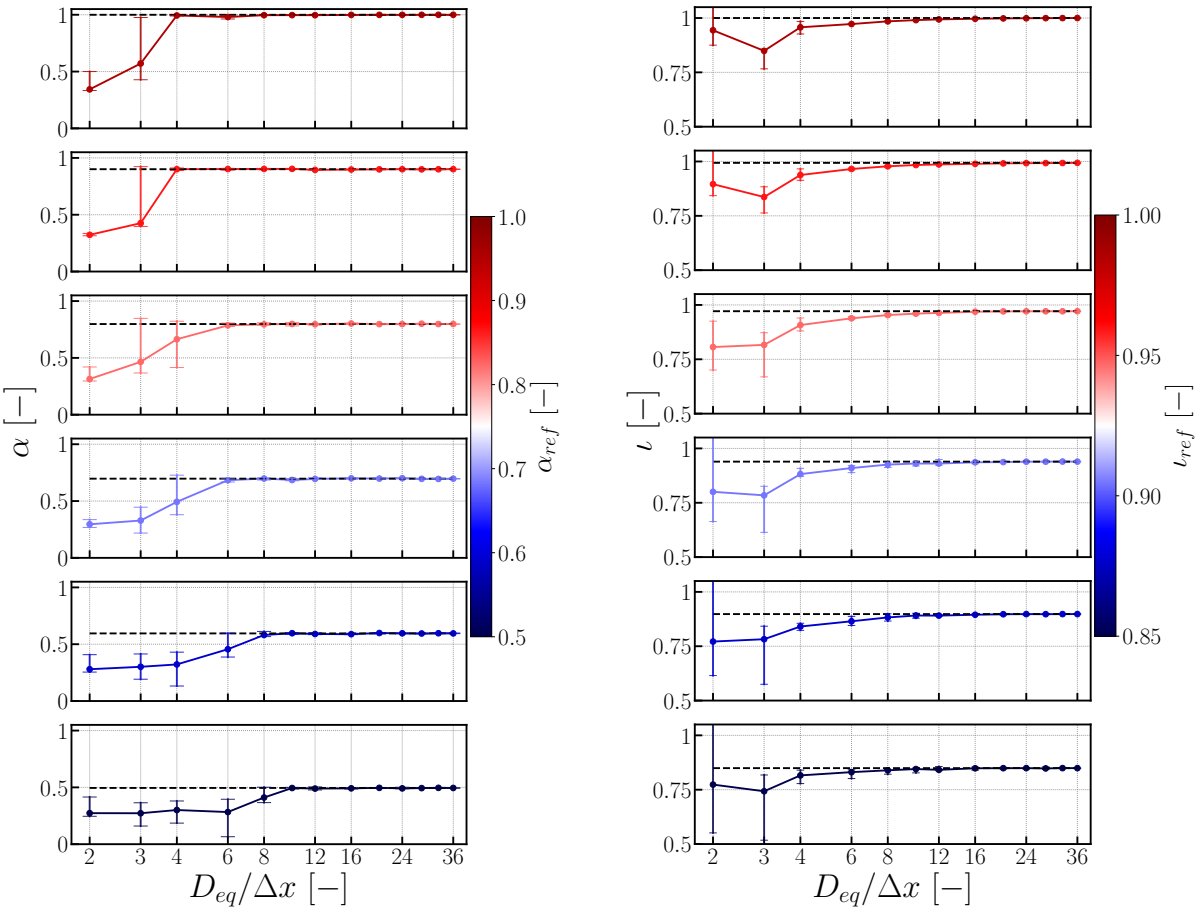

(a) Aspect ratio α

(b) Irregularity ι

Figure 7: Spatial convergence of the aspect ratio α, figure 7a, and the irregularity ι, figure 7b, for a spheroid varying $a : b$. Black dashed line is the reference value of the morphological parameter. The error bar indicates the maximum and minimum values obtained varying the location of the spheroid center.

$\phi > 0$ is for the liquid phase). The coefficient 6 has been fixed after some numerical test in our numerical solver. It prevents the reconstruction of a liquid droplet during the redistance step (Eq. 3).

4.1.6. Eulerian transformation: reconstruction of the velocity field

The transformation of the Eulerian droplet toward the Lagrangian droplet breaks the conservation of the momentum. Hereby reconstruction of the velocity field, Ling et al. [30] circumvent this inconsistency in the momentum equation. Their solution consists of defining a box centered on the particle and to modify the velocity field inside this box using a first order linear interpolation from the fluid cells' velocity at the faces of the box. This updated velocity field is divergence free only if the velocity at the faces of the box is divergence free and the divergence components are constant within the area of reconstruction. Figure 8 illustrates the reconstruction of the velocity field after the transformation of an Eulerian droplet.

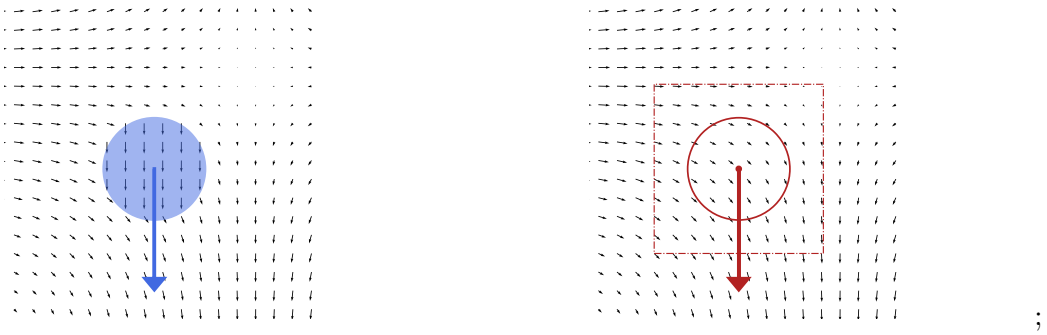

Figure 8: Reconstruction of the velocity field after the transformation of an Eulerian droplet (in blue) toward a Lagrangian droplet (in red). Red box indicates the area of reconstruction.

Although this transformation does not guarantee a solenoid vector field at the transformation step, it provides satisfactory results and is shown to enhance momentum conservation.

4.2. From the Lagrangian particle toward the Eulerian droplet

The Lagrangian droplets are allowed to transform toward Eulerian droplet to capture the interface topology changes arising from the coalescence of droplets in spray. The implementation is discussed within Section 4.2, with a special care on the reconstruction of the Eulerian fields at the transformation, and the main steps are summarized in algorithm 3.

4.2.1. Distance criterion $\mathcal{L}_P$

The distance from the center of the particle toward the closest interface is obtained through a linear interpolation at the position of the particle toward the level set field $\phi(\mathbf{X}_p)$. From

Algorithm 3: Eulerian-Lagrangian coupling: Lagrangian droplet transformation.

```
foreach Lagrangian droplet j do
    Compute distance to Eulerian droplets (Section 4.2.1)
    if Lagrangian droplet near Eulerian droplet then
        Add j to the Lagrangian droplets' transformation list
    end
end
foreach Lagrangian droplet in transformation list do
    Update VOF and level set fields (Section 4.2.2)
    Update Velocity field (Section 4.2.3)
    Remove Lagrangian droplet and add it to Eulerian droplet list
end
```

our analysis, the distance criterion $\mathcal{L}_P$ and $\mathcal{L}_D$ cannot be equal in order to avoid successive transformations from the Eulerian toward the Lagrangian frameworks. Therefore, the distance criterion $\mathcal{L}_P$ and $\mathcal{L}_D$ are set to

$$\mathcal{L}_D = 2\mathcal{L}_P,$$

to favor the transformation from Eulerian droplet toward Lagrangian particle.

4.2.2. Lagrangian transformation: reconstruction of the level set and the VOF

Reconstruction of the Eulerian fields

The reconstruction of the ICM fields at the Lagrangian toward Eulerian transformation has not been of particular interest in the literature. The update of the ICM method follows the general algorithm of the CLSVOF [16] (Section 2.1.1). The level set is reconstructed using a sphere equation, based on the radius of the Lagrangian droplet R_p. Next, the VOF is integrated over the new level set field, and the redistancing algorithm is used to recover the level set distance properties. This procedure is shown for a Lagrangian droplet (in red) moving toward an Eulerian droplet (in blue) in figure 9. Step 1 computes $\mathcal{L}_P$ from a linear interpolation of $\phi(\mathbf{X}_p)$. Following the transformation, Step 2 updates the Eulerian fields to account for the new Eulerian droplet. Step 3 is to iterate the redistancing algorithm until the level set distance properties are recovered.

Mass conservation improvement

The transformation from Lagrangian droplet toward Eulerian droplet yields to an over-estimation of the volume occupied by the droplet at the reconstruction of the interface step.

A line, or plane equation in 3D, is used to reconstruct the VOF based on the level set of a sphere. Although a minimization algorithm over a 9-point stencil, in 2D, is used to minimize the distance between the level set and the reconstructed line equation, a line equation cannot represent a parabolic surface. Therefore, the error on F for the kth cell is proportional to the numerical resolution, as illustrated in left figure 10 for a cell k.

To reduce the overestimation, we seek for the radius of reconstruction that minimizes the error $|V_D - V_p|$, with V_D and V_p the volumes of the reconstructed Eulerian droplet and Lagrangian droplet, respectively, considering two methodologies. The first one substitutes R_p by a radius R_p^*, obtained from a parametrization

$$R_p^* = R_p - \frac{1}{4}\Delta x^3 \,,$$

schemed in the left figure 10. The second relies upon an iterative Newton minimization algorithm to substitute R_p by an optimal value R_p^* that minimizes the error $|V_D - V_p|$. It consists in the reconstruction of the Eulerian fields, level set and VOF, over a fictitious domain, centered on the Lagrangian droplet centroid, of length $2D_{eq}$, to estimate the reconstructed volume V_D, satisfying an accuracy threshold.

Both implementations are tested along with the reconstruction of the ICM fields based on the true radius of the Lagrangian droplet. The numerical experiment consists of the transformation of a Lagrangian droplet varying both its numerical resolution, here in the range $D_p = 2\Delta x$ to $D_p = 12\Delta x$, and the centroid location (the center varies over the mesh spacing, as in the spatial convergence analysis of Section 4.1.4). The accuracy criterion of the Newton algorithm is set to

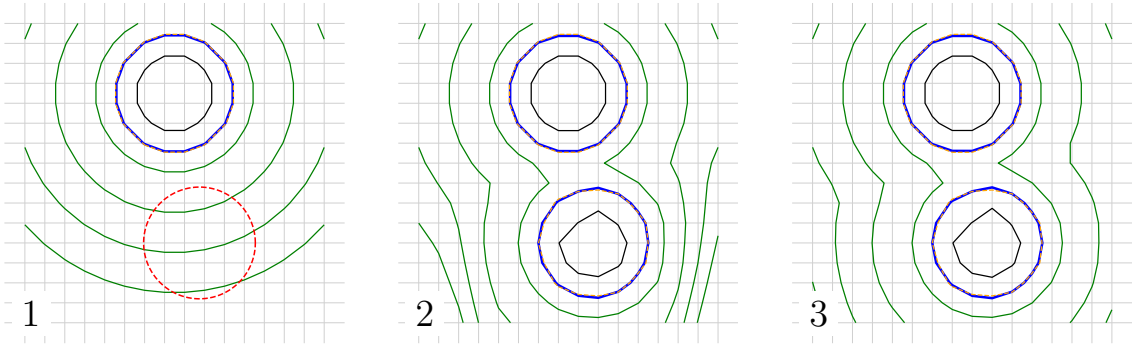

(a) Step 1: A Lagrangian particle in the vicinity of an Eulerian droplet.

(b) Step 2: modification of the Eulerian fields after Lagrangian transformation.

(c) Step 3: redistancing algorithm is used to recover the level set distance properties.

Figure 9: Transformation of a Lagrangian particle toward Eulerian droplet. Particle surface: red dashed line, level set levels: $\phi < 0$ solid green, $\phi = 0$ solid blue, $\phi > 0$ solid black, VOF planes: orange dashed line.

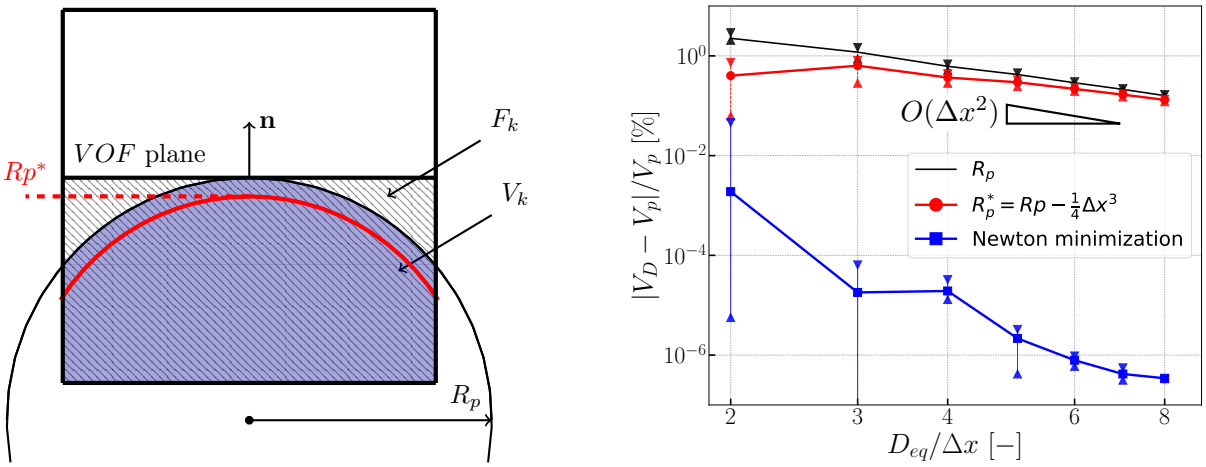

Figure 10: Error on the volume conservation. Left: volume fraction reconstruction from the level set (Section 2.1.1). Right: Spatial convergence error $|V_D - V_p|$.

10^{-5}, the maximum number of iterations to 10.

The results of the spatial convergence of the volume variation $|V_D - V_p|$ is shown in figure 10. The results of the ICM and the R_p^* substitution converge with a second order of spatial accuracy. In addition, the results using R_p^* always improves the volume conservation, for example at coarse numerical resolution, $D_p/\Delta x = 2$, the error is reduced of one order of magnitude with respect to the ICM. The results obtained with the Newton minimization algorithm always significantly improve the mass conservation regardless of the numerical resolution for a reasonable number of iterations.

In the manuscript, the Newton minimization algorithm is used for the simulations of validation. For the analysis of the jet, the retraction of the radius methodology is used to reduce the overall computational cost in massively parallel simulations.

4.2.3. Lagrangian transformation: reconstruction of the velocity field

At Lagrangian transformation, the velocity field is reconstructed as in Ling et al. [30]. It consists in setting the velocity of the particle within the fluid cells *inside* the reconstructed Eulerian droplet. They also account for the flow disturbance induced by the two-way coupling and propose a correction to filter this disturbance. This correction is natural to our framework because the flow disturbance correction derived in Evrard et al. [38] is used.

4.3. Eulerian-Lagrangian coupling with the two phase flow solver

The coupling between the flow solver and the Eulerian-Lagrangian framework is presented as a flow chart in figure 11. The classical time loop for our flow solver, that includes the transport

of interfaces, transport of Lagrangian droplets, resolution of the Navier-Stokes equations with the projection method, the Eulerian-Lagrangian coupling is applied.

The methodology follows the organization of Section 4.1 for the Eulerian droplets and Section 4.2 for the Lagrangian droplets. The values used for the criteria of transformation, presented in Sections 4.1 and 4.2 are summarized in table 1. The droplets qualifying for transformation are stored in a general list, used to reconstruct the Eulerian fields. Then, the list storing the droplets' information is updated and shared with neighboring processors. This step concludes the current time step.

Criterion	**Symbol**	**Value**	**Definition**
From Eulerian droplet toward Lagrangian droplet			
Numerical resolution	ϵ_V	4.	Section 4.1.2
Distance from other Eulerian droplets	$\mathcal{L}_D$	$2D_{eq} \geq \mathcal{L}_D$	Section 4.1.3
Aspect ratio	ϵ_α	0.65	Section 4.1.4
Irregularity	ϵ_ι	0.85	Section 4.1.4
From Lagrangian droplet toward Eulerian droplet			
Distance from other droplet	$\mathcal{L}_P$	$\mathcal{L}_P \leq \mathcal{L}_D/2$	Section 4.2.1

Table 1: Summary of the criteria of transformation for Eulerian toward Lagrangian droplets transformation, and vice-versa.

5. Validation

5.1. Particle to Droplet and Droplet to Particle transformations

5.1.1. Numerical configuration

In this numerical experiment successive transformations from Lagrangian droplets to Eulerian ones are studied to validate the reconstruction of the interface for a large number of transformations in both directions. The coupling with the flow solver is deactivated and only the level set and the VOF fields are modified at the transformation.

100,000 mono dispersed Lagrangian droplets are randomly initialized within a unit cubic box, allowing the particle to overlap but to touch the borders of the domain. The total number of cells is 384^3, with $D_p/\Delta x = 3.84$.The thresholds used for the transformation are listed in table 1. In order to emphasize transformation, both distance distance criteria are set to $\mathcal{L}_P = 2\Delta x$ and $\mathcal{L}_D = 2\Delta x$.

5.1.2. Results

The fields at initialization, after transformation toward Eulerian droplets, and after the reverse transformation from Eulerian toward Lagrangian droplets, are shown in figure 12. From

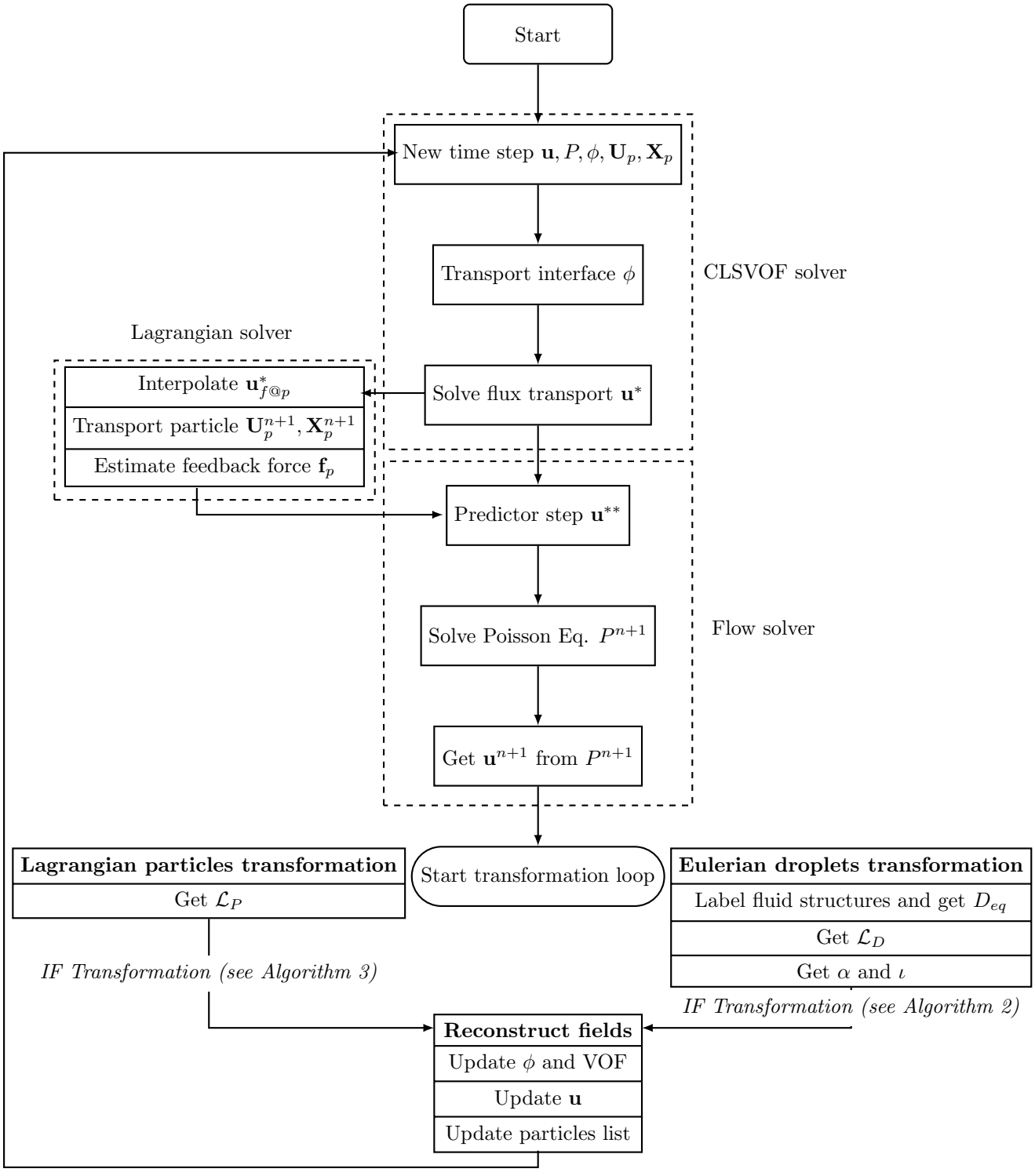

Figure 11: Flow chart of the Eulerian-Lagrangian coupling within the flow solver.

the 100,000 initialized Lagrangian droplets, only 26,640 isolated structures are identified after Eulerian transformation and structure detection through the labeling algorithm because of the initial overlaps. An example of overlapping liquid structure is given in figure 13.

The shape analysis of the 26,640 Eulerian droplets is plotted in figure 14. From the scattering

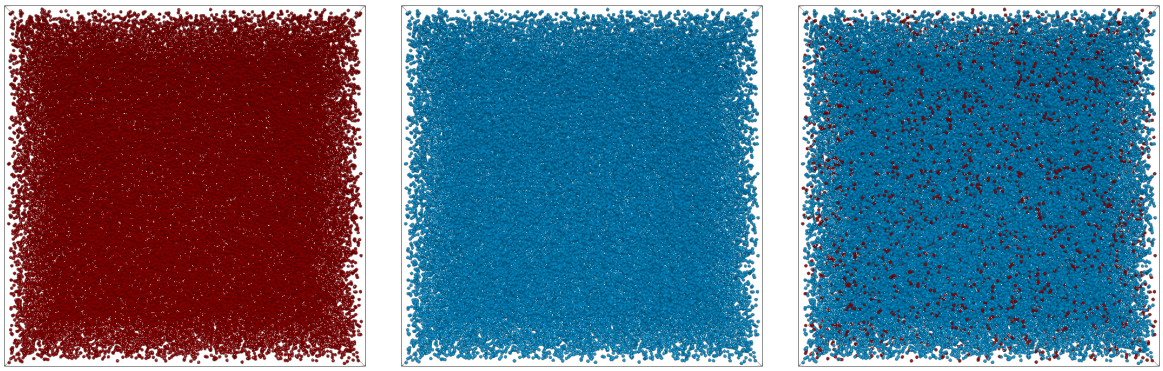

Figure 12: Left: Initialization of Lagrangian droplets (in red), center: Lagrangian droplets are transformed to droplets (in blue), right: selected droplets are transformed back toward Lagrangian droplets.

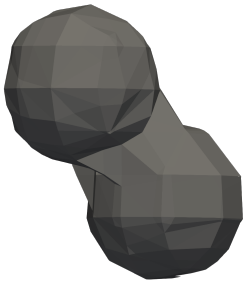

Figure 13: Overlapping liquid structures identified after transformation from Lagrangian toward Eulerian droplet.

of points, the droplets are classified in three populations, i) droplets qualifying for transformation, ii) droplets within the range $0.2 < \alpha \leq 0.65$, iii) droplets with $\alpha \leq 0.2$ and $\iota \leq 0.8$. In population i) the droplets are close to the initial sphere, as seen with their volume in the range $1 \leq V_D/V_P < 1.2$. At $V_D/V_P = 1$, the minor deviations from the ideal value of ι and α for a sphere are to be expected due to the numerical resolution (Section 4.1.4). In population ii) most of the droplets have a volume in the range $1.2 \leq V_D/V_P < 10$ (see extracted structure from the numerical simulation in figure 13), the morphological criteria do not qualify these droplets for transformation. Population iii) is composed of large overlapping structures, or groups of structures. The combination of the two morphological criteria allows us to accurately discriminate against these structures.

The transformation from Eulerian toward Lagrangian droplets identifies 31.6% of Lagrangian droplets and 68.4% of isolated Eulerian droplets (right figure 12). The average radius of these Lagrangian droplets is 5.11×10^{-3}, this represents an increase of 2.2% with respect to the initial Lagrangian droplet.

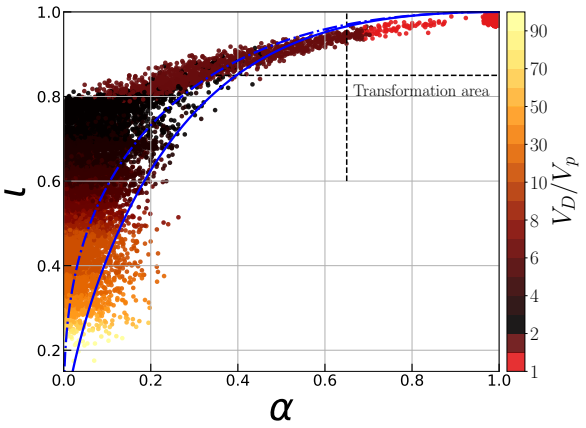

Figure 14: Irregularity parameter, ι, against aspect ratio, α, for all the transformed droplets. The color map represents the volume of the droplet scaled by the maximum volume identified. Dashed black line represents the value set for the two morphological criteria. Blue solid and dashed lines are the analytical relation between α and ι for a prolate and an oblate spheroid, respectively [51].

5.2. Transformation of a free-falling confined droplet

5.2.1. Numerical configuration

The second validation case considers the transformation of a free-falling Eulerian droplet toward a Lagrangian droplet. The numerical configuration is similar to Section 3. The Eulerian droplet is transformed toward Lagrangian droplet at three transformation times, $t_{trans} = 1.25t/\tau_p$, $3.125t/\tau_p$ and $5t/\tau_p$, which corresponds to two distinct stages of acceleration evolution and a stationary droplet, respectively. The motivation is to study the influence of the transformation over the free-falling droplet evolution and its terminal velocity.

The numerical resolution of the Eulerian droplet is $D_D/\Delta x = 4.8$. The transformation is done toward both the one way and two way coupling, using the best parameters resulting from Section 3, *i.e.* an interpolation/spreading kernel as large as the computational domain permits coupled with the correction of the self-disturbance in the two way coupling.

5.2.2. Results

The temporal evolution of the transformed free-falling droplet is reported in figure 15, for the three characteristic times of transformation and both methods. A zoom on the transformation time is added for each graph showing the temporal evolution of the position, velocity, and acceleration of the particle for a few time steps after transformation.

For all transformation times, the one way method accelerates the Lagrangian droplet, resulting in increasing the speed of the droplets after transformation. The transformation toward the two way coupling ensures the continuity of the velocity profile at the transformation time;

a continuous evolution for both the acceleration and the velocity of the Lagrangian droplet is observed.

For all test cases the transformation from Eulerian toward Lagrangian reduces the computational time of the simulation. The CFL restriction defined on the curvature being the most restrictive, removing the interface allows larger time steps.

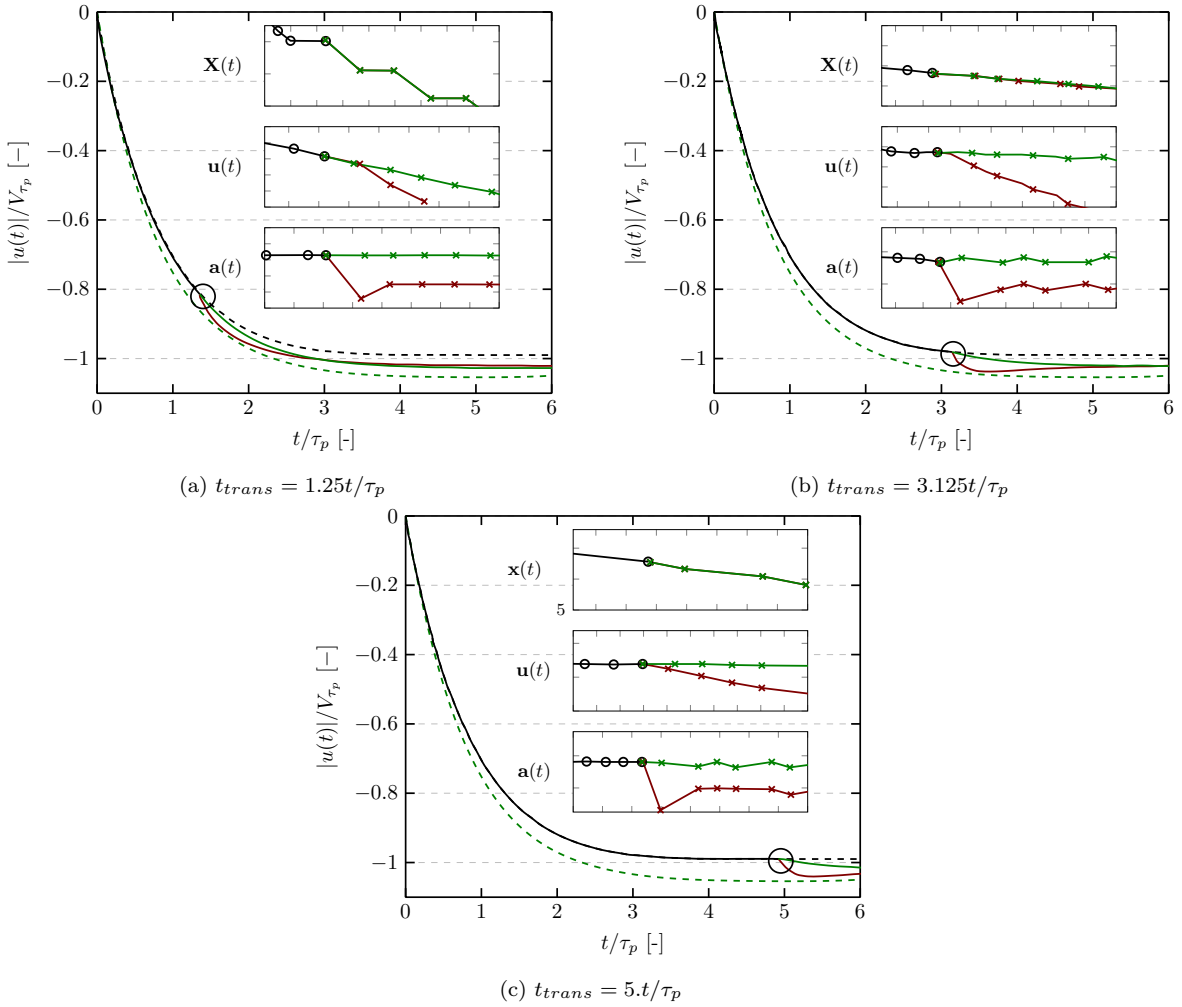

(a) $t_{trans} = 1.25t/\tau_p$

(b) $t_{trans} = 3.125t/\tau_p$

(c) $t_{trans} = 5.t/\tau_p$

Figure 15: Temporal evolution of the velocity of a transformed free-falling droplet. Three transformation time are shown $t_{trans} = 1.25, 3$ and $5t/\tau_p$. A zoom on the transformation time is proposed, showing the temporal evolution of the acceleration, the velocity, and the position of the particle for a few time steps. Solid black line: ICM, solid green line: two way, solid red line: one way. The dash lines are the pure ICM and two way references.

5.3. Decaying Homogeneous Isotropic Turbulence

5.3.1. Numerical configuration

This validation case considers the transformation of Eulerian droplets subject to complex flows. The goal is to compare the results of the Eulerian-Lagrangian coupling method to the coarse ICM in a complex flow. The turbulent flow field is generated as in Duret et al. [52] and Canu et al. [19] using a linear forcing [53]. The mean kinetic energy $\overline{k}_c$ is set to $\overline{k}_c = 3.6$

m^2/s^2, the fluctuating velocity $u^{'}$ to $u^{'} = \sqrt{\frac{2}{3}\overline{k}_c}$, and the eddy turnover time T_e to $T_e = u^{'}/\Lambda$ with Λ being the Taylor length scale set to half the domain length. The physical size of the domain, and the physical properties of both phases are reported in table 2. This set of physical parameters gives an inertial Taylor length scale based Reynolds number of $Re_\Lambda = \Lambda\sqrt{\frac{2\overline{k}_c}{3}}/\nu_f = 37.77$, a liquid Weber number of $We_D = \frac{\rho_f D_D (u^{'})^2}{\sigma} = 1.60$, which ensures that the droplets remain spherical, and a Stokes number of $St = \tau_p/T_e = \rho_f D_D^2/18\mu_g \times \overline{u^{'}}/L_c = 2.58$.

These non-dimensional numbers are reported in table 3 along with the relevant characteristic times: the eddy turnover time T_e, the particle relaxation time τ_p and, the collision time $\tau_c = \left[4N_D D_D^2 \sqrt{\pi(\overline{u^{'}})^2}\right]^{-1}$, where N_D is the total number of droplets. To limit coalescence the liquid volume fraction is set to 0.1%, giving $N_D = 64$. The total number of fluid cells is 128^3, it results in 4 fluid cells across the diameter of the Eulerian droplets.

ρ_f $[\frac{kg}{m^3}]$	ρ_g $[\frac{kg}{m^3}]$	μ_f $[\frac{kg}{m.s}]$	μ_g $[\frac{kg}{m.s}]$	σ $[\frac{kg}{s^2}]$	L $[m]$	Δx $[-]$	D_D $[m]$	$D_D/\Delta x$ $[-]$
1945.0	65.0	5.650×10^{-4}	1.879×10^{-5}	1.35×10^{-2}	1.5×10^{-4}	1.172×10^{-6}	4.69×10^{-6}	4

Table 2: Physical parameters employed in the Decaying Homogeneous Isotropic Turbulence configuration.

Re_Λ $[-]$	Λ $[m]$	ϕ [%]	N_D $[-]$	We_D $[-]$	T_e $[s]$	τ_p $[s]$	τ_c $[s]$	St $[-]$	$\overline{k}_c$ $[\frac{m^2}{s^2}]$
37.77	7.064×10^{-6}	0.10	64	1.60	4.885×10^{-5}	1.25×10^{-4}	1.5×10^{-8}	2.58	3.6

Table 3: Relevant non dimensional parameters of the Decaying Homogeneous Isotropic turbulence configuration.

A specific methodology is employed to initialize the two phase flow turbulence in order to prevent strong shear at the Eulerian droplets' interface [54]. A single phase flow is initialized forcing the gas phase during $5T_e$. Then 64 equally spaced fixed resolved particles are added in the domain using the immersed boundary method of Uhlmann [55] that resolves all fluid-surface interactions. The forcing scheme is held during $2Te$ to adapt the flow to the particles. Then, the forcing is stopped and the resolved particles are transformed toward moving Eulerian droplets. At $8T_e$ the Eulerian droplets are transformed toward Lagrangian droplets, and statistics over three realizations performed per method are studied, until the turbulent kinetic energy drops to 50% of the energy at $8T_e$.

5.3.2. Results

The trajectory of Eulerian/Lagrangian droplets starting at the transformation time is shown in figure 16. The position at the transformation, $\mathbf{X}_{p,trans}$ is used as a reference to normalize the

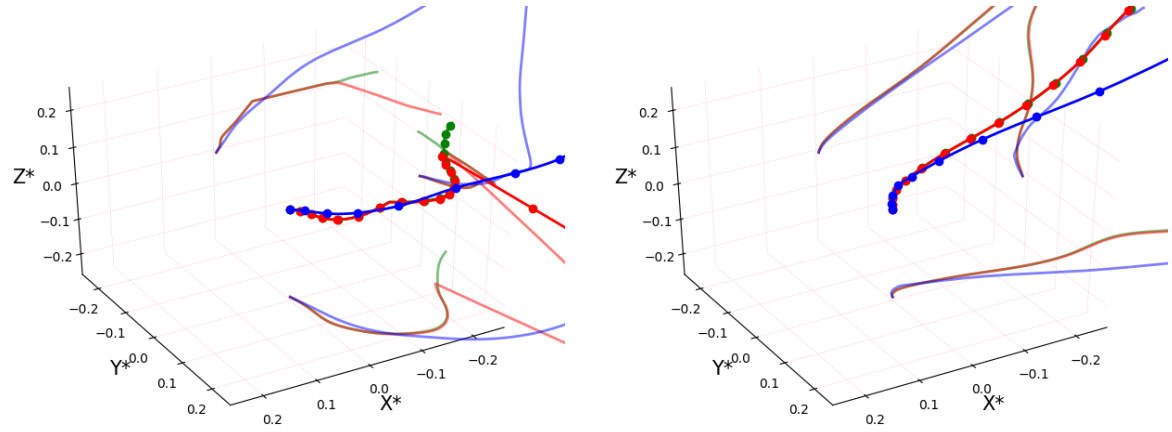

Figure 16: The droplets temporal position evolution after transformation for the ICM (blue), Eulerian-Lagrangian coupling one way (red) and two way (green). The solid lines with markers: 3D trajectory, solid lines without markers: 2D projection.

spatial evolution

$$\mathbf{X}^* = \left(X_p(t) - X_{p,trans}\right)/L\,. \tag{35}$$

The trajectory of the droplets at the time after the transformation is similar for all methods. However, the trajectory of the ICM droplets deviates from the trajectory of the droplets transported within the Lagrangian framework several time steps after the transformation. Differences in trajectory are also observed between both Lagrangian frameworks.

The temporal evolution of the averaged dispersion, defined

$$< |\mathbf{X}_D(t) - \mathbf{X}_D(t_{trans})| >= \frac{1}{N_D}\sqrt{\left[\sum_{i=1}^{N_D} |\mathbf{X}_{D,i}(t) - \mathbf{X}_{D,i}(t_{trans})|\right]^2}\,, \tag{36}$$

and the root-mean-square velocity, V_{RMS},

$$V_{RMS}(t) = \frac{1}{N_D}\sqrt{\left[\sum_{i=1}^{N_D} |\mathbf{u}_{D,i}(t)|\right]^2}\,, \tag{37}$$

are reported in figure 17. The Eulerian-Lagrangian coupling increases the dispersion of the Lagrangian droplets with respect to the ICM. The comparison of both Lagrangian approaches show that the Lagrangian droplets transported within the one way framework have a lower dispersion than the two way framework; this is a result of the modeling approach. The V_{RMS} analysis shows that the ICM method reaches a higher peak, meanwhile the results obtained with the Eulerian-Lagrangian coupling overlap. Thus, in complex flow configuration, the comparison

of the Eulerian-Lagrangian coupling with the under-resolved ICM shows a modification of the droplets' statistics that can be impeded to the poor resolution of the ICM droplets.

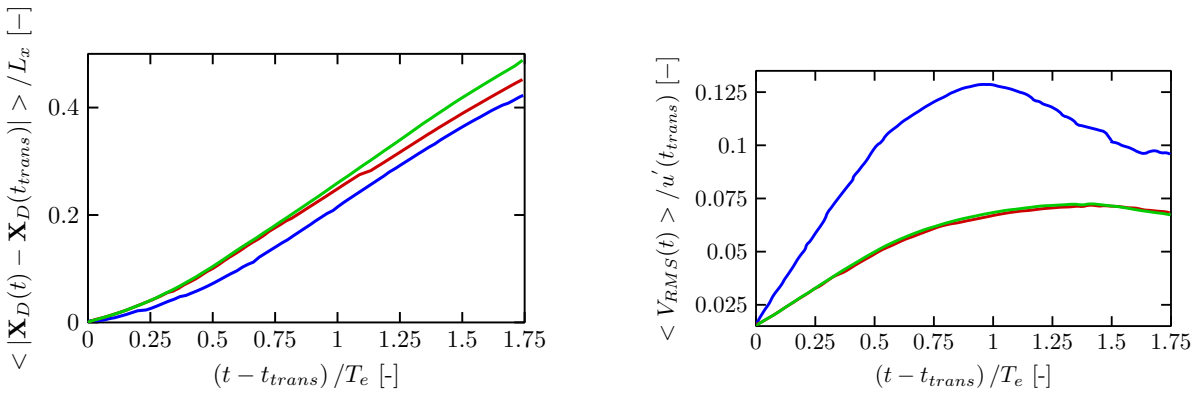

Figure 17: Mean position evolution (left) and V_{RMS} (right) against characteristic time. ICM (blue), Eulerian-Lagrangian coupling one way (red) and two way (green).

6. Eulerian-Lagrangian coupling applied to cross flow atomization

6.1. Numerical configuration

The Eulerian-Lagrangian coupling is applied to the analysis of a jet in cross flow, relevant to several industrial applications [56]. The configuration consists of the injection of a turbulent liquid jet bent under the action of a perpendicularly injected uniform flow. This configuration produces a large number of droplets, as reported both experimentally in Aalburg et al. [57], Brown and McDonell [58] and numerically in the work of Herrmann [59], Xiao et al. [60] as well as within our research group [20].

The fluid physical properties are set to $\rho_f = 12.25\ kg/m^3$, $\mu_f = 1.11 \times 10^{-4}\ kg/(m.s)$, and the gas carrier phase to $\rho_g = 1.225\ kg/m^3$, $\mu_g = 1.82 \times 10^{-5}\ kg/(m.s)$. The surface tension is set to $\sigma = 7 \times 10^{-2}\ N/m^2$. The size of the computational domain is $[-10 \times D_{inj} : 30 \times D_{inj}, -5 \times D_{inj} : 5 \times D_{inj}, 0 : 20 \times D_{inj}]\ m$, where D_{inj} is the diameter of injection set to $D_{inj} = 1.3 \times 10^{-3}\ m$. The injection point is located at $[0, 0, 0]$. The turbulent pipe flow profile is obtained using filter based turbulent data generation [61], with a mean velocity of $U_{inj} = 97.84\ m/s$. The carrier velocity is uniform and set to $U_c = 120.4\ m/s$. This set of physical parameters gives the characteristic numbers reported in table 4.

We use a total of 16.7×10^6 fluid cells, resulting in 14.5 cells across the diameter of injection. This results in a coarse description of the jet, but sufficient to our numerical analysis. The boundary conditions are: inflow and outflow in the streamwise direction (x-component), wall in

ρ^*	M	We_j	Re_j	We_c	Re_c
10	6.6	2178	14,079	330	10,652

Table 4: Cross flow atomization's characteristic dimensionless numbers, density ratio $\rho^* = \rho_f/\rho_g$, momentum ratio $M = \rho_f U_{inj}^2/\rho_g U_c^2$, the injection Weber number $We_j = \rho_f D_{inj} U_{inj}^2/\sigma$, the injection Reynolds number $Re_j = \rho_f D_{inj} U_{inj}/\mu_f$, the carrier Weber number $We_c = \rho_g D_{inj} U_c^2/\sigma$ and the carrier Reynolds number $Re_c = \rho_g D_{inj} U_c/\mu_g$.

the direction of the liquid injection (y-component) except at the liquid jet injection (bottom) and free slip in the spanwise direction (z-component). The simulation is performed during $4 \times t^*$ where t^* is a characteristic time based on the droplets' residence time in the domain, $t^* = tU_c/(30D_{inj}) = 3.24 \times 10^{-4}\ s$.

Three configurations are compared, the ICM approach, the Eulerian-Lagrangian coupling with the one way and the two way methods. The criteria of transformation from droplets toward particles and vice-versa are listed in table 1. The morphological parameters are not checked when the droplet has less than 2 fluid cells across the diameter; these droplets are directly transported within the Lagrangian framework.

6.2. Analysis of the transformation criteria

To study the transformation criteria relying on the sphericity of the droplets, the irregularity and the aspect ratio of all the droplets in the ICM simulation are computed. The results are shown in figure 18a where the color map indicates the droplet diameter to fluid mesh size ratio (here for clarity only 10% of the droplets are shown). The population of droplets within the range $D_{eq}/\Delta x \leq 2$, (in red), spreads from $\alpha = 0$ to $\alpha = 0.85$. A large part of these droplets validate the morphological criteria of transformation. The droplets in the range $2 < D_{eq}/\Delta x \leq 4$, (in blue), spread along the spheroid relations derived in Chéron et al. [51], and are in the range $\alpha = [0, 0.85]$, and $\iota = [0.4, 1.]$. Several droplets are identified within the transformation area, these droplets are expected to be transported using the Lagangian method within the Eulerian-Lagrangian coupling. The largest droplets, (in black) are identified in the range $0.2 \leq \alpha \leq 0.4$; $0.3 \leq \iota \leq 0.5$; they are large ligaments observed near the breakup area and are transported with the resolved interface method.

The transformation criteria implies that the droplets remain spherical within the simulation time. The droplet Weber number can be used to indicate the probability to break of a droplet, defined as

$$We = \frac{\rho_g D_{eq} |\mathbf{u}_D - \mathbf{U}_c|^2}{\sigma},$$

where $\mathbf{u}_D$ is the velocity of the droplet and, $\mathbf{U}_c$ is the cross flow velocity. The Weber is plotted only for the droplets satisfying the morphological criteria of transformation against their distance to the injection point in figure 18b (here for clarity only 50% of the droplets are shown). The results indicate that the further from the injection point, the lower is the Weber number of the droplets. Moreover, most of the droplets have a Weber number below $We < 12$; thus these droplets are not likely to break [62], and are good candidates for transformation.

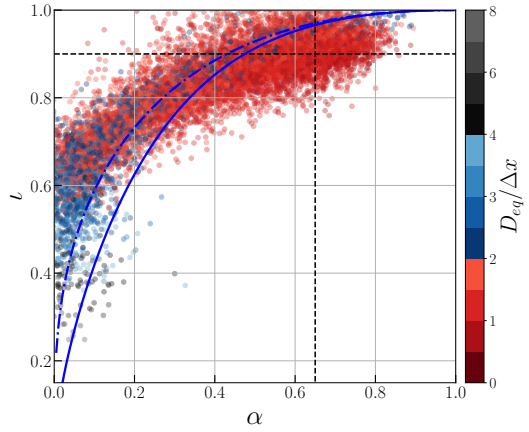

(a) Irregularity parameter, ι, against aspect ratio, α, for all structures in the spray. The color map represents the volume-based-equivalent diameter scaled by the mesh spacing. Blue solid and dashed lines are the analytical relation between α and ι for a prolate and an oblate spheroid, respectively [51]. Black dashed lines represents the morphological criteria limits.

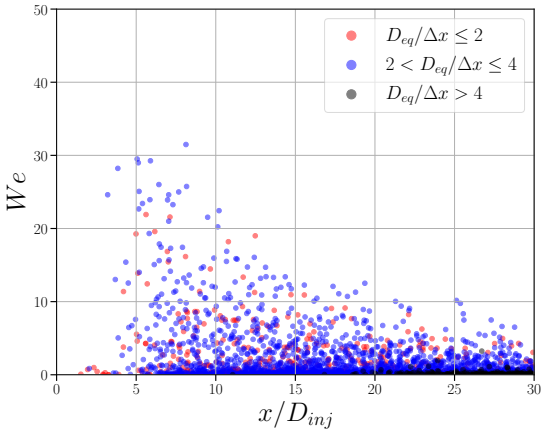

(b) Spatial evolution of the droplets' Weber number for droplets validating morphological criteria (figure 18a). Colored markers indicate droplets candidate to transformation.

Figure 18: Morphological and physical analysis of the droplets produced in the reference ICM simulation.

6.3. Analysis of the Eulerian-Lagrangian coupling

6.3.1. Qualitative analysis

A snapshot of the developed atomized jet is presented in figure 19 for the ICM configuration and the Eulerian-Lagrangian coupling (one way). In this figure we observe the bending of the turbulent liquid jet under the action of the aerodynamic force induced by the cross flow [63], and the flattening of the jet in the direction normal to both the cross flow and the liquid injection. Two phase flow instabilities are observed on the liquid column. They propagate over the surface of the jet until the breakup of the liquid column, generating several large ligaments in the primary atomization area [64]. These large ligaments can further break into smaller droplets under aerodynamic shear effects. This results in a poly-dispersion of the droplets' size. In the bottom figure, corresponding to the Eulerian-Lagrangian coupling results, it can be seen that the majority of the small droplets are transported within the Lagrangian framework (white color), and the large structures are accurately resolved with the ICM (red color).

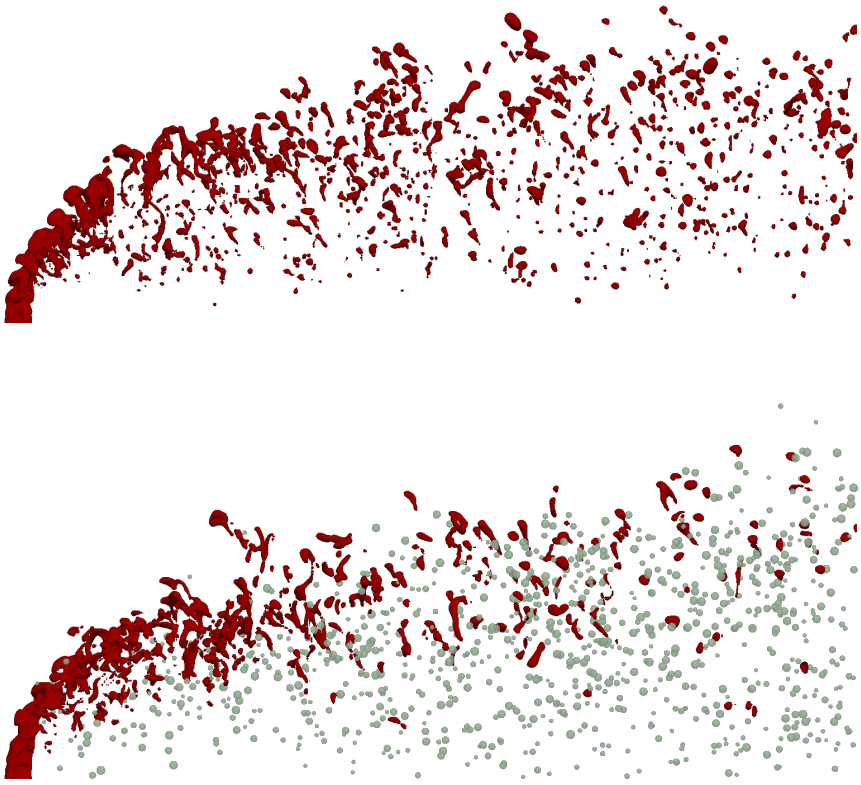

Figure 19: ICM (top) and Eulerian-Lagrangian coupling one way (bottom) snapshots of the side view of the cross flow atomization simulation. Dark color represents the iso-zero level of the ICM method, light color represents the surface of the spherical Lagrangian particles.

From figure 19 we identify three 'states', the liquid core that is the continuous liquid column until breakage $\mathcal{S}_{core}$, the dispersed phase characterized by the droplets $\mathcal{S}_D$, and the carrier phase $\mathcal{S}_g$. These three states are identified using the labeling algorithm, Section 4.1.1. They are classified as follow

$$\begin{aligned} \mathcal{S}_g &= 1 - F_k \\ \mathcal{S}_{core} &= F_k \quad \text{if } \mathcal{X}_k = \mathcal{X}_{core} \\ \mathcal{S}_D &= F_k \quad \text{if } \mathcal{X}_k \neq \mathcal{X}_{core} \end{aligned}$$

where $\mathcal{X}_{core}$ is the label of all the fluid cells connected to the jet injection.

In the Eulerian-Lagrangian coupling, the dispersed phase can be divided further among two categories, the droplets transported within the ICM framework and the Lagrangian droplets. The volume occupied by the liquid core, the ICM droplets and Lagrangian droplets is temporally averaged, and, the results are reported in table 5 for the ICM, and the two Eulerian-Lagrangian couplings. The liquid volume occupied per categories are similar for all configurations.

Method	**Liquid Core** [%]	**ICM droplets** [%]	**Lagrangian particles** [%]
ICM	36.76	63.23	-
Eul-Lag one way	32.05	35.58	32.37
Eul-Lag two way	35.54	34.68	29.78

Table 5: Liquid volume occupied by the liquid core, droplets transported within the ICM framework and droplets transported with the Lagrangian framework for the three studied configurations applied to the cross flow atomization.

6.3.2. Quantitative analysis

From the qualitative analysis of the primary atomization area, a quantitative analysis can be drawn using an entropy-based probability function [65], using the definition of 'states' to which the fluid cell belongs: $\mathcal{S}_{core}$, $\mathcal{S}_G$, $\mathcal{S}_D$. The number of states seen by each fluid mesh are temporally averaged over all the time steps to determine the probability of occurrence of each state, referred to as p_S. The regions upstream to the jet are more likely to see exclusively the carrier phase, therefore having a null entropy. The same comments hold for the area of the liquid jet injection. On the other hand, regions where the breakup occurs are more likely to identify the three states, and, the maximum entropy is reached when

$$p_{\mathcal{S}_{core}} \approx p_{\mathcal{S}_D} \approx p_{\mathcal{S}_g},$$

which is used to normalize the entropy field,

$$\text{Entropy} = \frac{-\sum_{\mathcal{S}} p_{\mathcal{S}} \ln p_{\mathcal{S}}}{\ln 3}.$$

To identify the primary atomization area the three state entropy threshold defined in Blaisot and Yon [65] is used, Entropy $= \frac{\ln 2}{\ln 3} \approx 0.631$, that captures the regions where each of the three states are located. The projection of the 3D Entropy field is done over the wall-normal and spanwise direction, see figure 20. The co-ordinates of the droplets transformed into particles for the two way Eulerian-Lagrangian coupling are also added (only 25% of the total number of events is shown for the readability of the figure). Only two way transformation co-ordinates are reported, since the one way and two way Eulerian-Lagrangian couplings' results do not vary.

The spanwise projection of the Entropy shows the conic shape of the liquid core (Entropy = 0). The three states entropy contour indicates the presence of the three states near the injector, which corroborates the creation of droplets near the injector. This area expands from the liquid core limits to downstream to the jet. Also, the further from the injection point, the further the high entropy area is from the bottom wall. This agrees with the observations on the snapshot of the atomization in figure 19. Similarly to the spanwise projection, the wall-normal projection indicates a null entropy area where only the carrier phase is identified (Entropy = 0, bottom and top left corners). This area reduces along with the expansion of the jet, and thus the high entropy area. The co-ordinates of the Eulerian droplets' transformation indicate that there are few transformations near the liquid jet, and that the majority of the transformation occurs near or within the high entropy area.

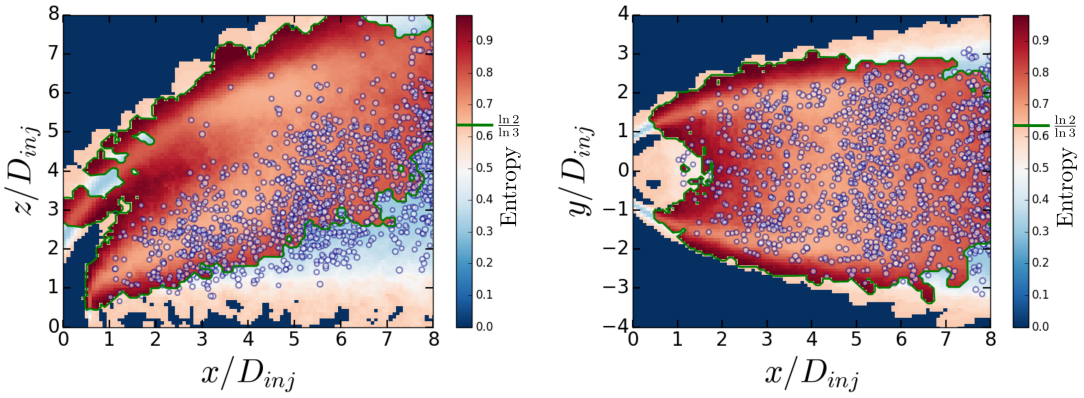

Figure 20: Entropy projection over the spanwise (left) and wall-normal (right) directions. Solid green: contour of the three state entropy threshold Entropy ≈ 0.631. Markers indicate the co-ordinates of transformation of the Eulerian droplets (two way Eulerian-Lagrangian coupling).

6.3.3. Dispersed phase analysis

The results reported in figure 19 show a larger number of Lagrangian particles near the end of the computational domain than the Eulerian droplets. To quantify these qualitative differences the droplets' size distributions functions at $x/D_{inj} = 5, 10$ and 20, using a log-space base, are reported in figure 21 along with the results of the ICM configuration. At $x/D_{inj} = 5$ and 10 several Eulerian droplets have been transformed into Lagrangian droplets, this coincides with the results shown in figure 20. These Lagrangian droplets are exclusively in the range $D_{eq}/\Delta x = [1; 4]$ and represent the majority of the droplets in this range. The comparison with the ICM results show similarities in the histograms. At $x/D_{inj} = 20$ the probability to find small Eulerian droplets in the ICM configuration decreases, meanwhile it remains constant in the Eulerian-Lagrangian coupling. The ICM fails to transport these small droplets downstream to the jet as they break into smaller structures that results in numerical artifacts, removed with the VOF restriction (Section 2.1.1). In the Eulerian-Lagrangian coupling these droplets are transported, it results in a larger number of small droplets in this simulation, which explains the higher probability to find large droplets in the ICM framework.

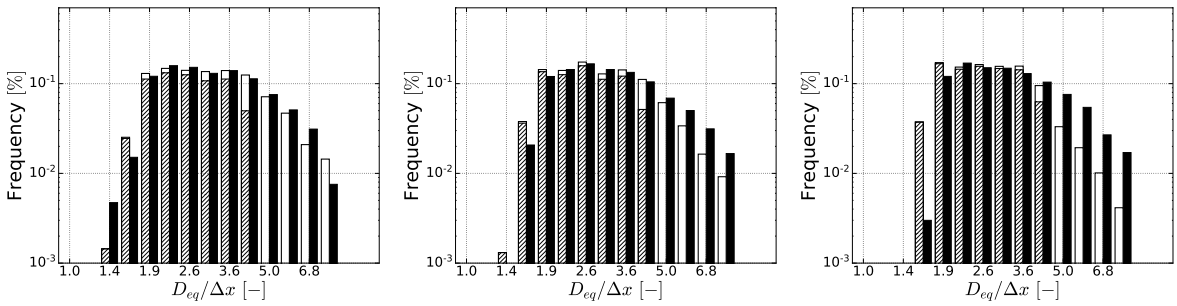

Figure 21: Frequency distribution of the volume-based-equivalent diameter scaled by the mesh spacing at several distances of injection $x/D_{inj} = [5, 10, 20]$. ICM: filled bars, Eulerian-Lagrangian coupling one way - ICM droplets: white bars, Lagrangian droplets: hatch bars.

The analysis of the temporal evolution of a free-falling confined particle shows that the method and the numerical resolution influence the velocity evolution, Section 3. Thus, we report in figure 22 the frequency distribution of the velocity of the Eulerian/Lagrangian droplets for the three studied configurations in the range $0. \leq D_{eq}\Delta x \leq 4.$.These figures show the velocity components in the cross flow direction (u_p) and the spanwise direction (w_p), respectively. Both plots are scaled by the cross flow velocity. For all methods, the u_p component is centered on $u_p/U_c = 1$ showing that the droplets evolve at the speed of the cross flow; these droplets behave as tracers and agrees with the previous observations of Herrmann [39]. The dispersion in the

spanwise direction, w_p/U_c, is centered on 0 for all methods, as observed in the work of Herrmann [39]. However, their results show a larger dispersion of small droplets that is not found in our work due to the low numerical resolution used. The use of the Eulerian-Lagrangain two way coupling slightly reduces the concentration of the droplets at $w_p/U_c = 0$.

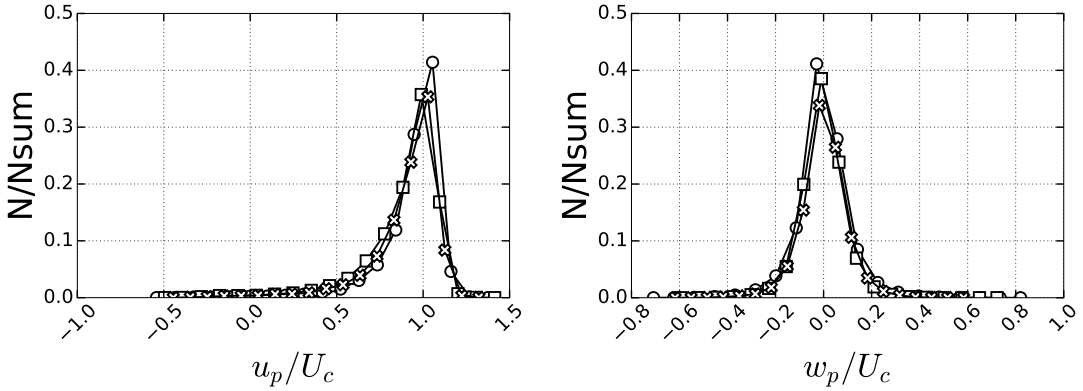

Figure 22: Velocity distribution in the streamwise (left) and the spanwise (right) directions scaled by cross flow injection velocity for the droplets in the range of transformation $0. \leq D_{eq}\Delta x \leq 4.$. ICM: circle markers, Eulerian-Lagrangian one way: square markers, Eulerian-Lagrangian two way: cross markers.

6.4. Computational cost

The computational time spent in the flow solver per configuration is analyzed for the fully developed jet. Here the total CPU time is split in five main groups: the Lagrangian solver, the transformations, the transport of the interface [18] (ICM), the iterative resolution of the Poisson equation, and, the other functions related to the Eulerian framework such as the projection method or the time spent in the output writing (Others). The total time spent for $0.2t^*$ characteristic time per method and groups are reported in table 6. The methods considered are the ICM and the Eulerian-Lagrangian couplings. For all configurations the most significant computational efforts are in the transport of the interface/flux, the Other functions related to the Eulerian framework, and the Poisson solver. The implementation of the transformation algorithm from Eulerian toward Lagrangian and vice-versa is negligible compared to the total CPU time.

The comparison between ICM and Eulerian-Lagrangian couplings do not exhibit a computational gain or increase for the transport of interface, or resolution of the solver. However, the comparison of the Eulerian-Lagrangian couplings show that the time spent in the Lagrangian function for the two way coupling significantly increases the CPU time, meanwhile the one way coupling CPU computational cost is negligible. Most of this time is spent in sequential: in the

Method	ICM $[s]$	Trans. $[s]$	Lag. $[s]$	Poisson solver $[s]$	Others $[s]$	Total $[s]$
ICM	740.21	-	-	546.19	799.62	2102.38
- MPI	512.76	-	-	223.62	517.41	1253.79
Eul-Lag one way	727.25	0.09	0.24	515.79	787.07	2031.70
- MPI	474.98.27	0.04	0.05	198.61	485.33	1381.74
Eul-Lag two way	793.45	0.12	336.29	533.43	856.26	2520.12
- MPI	531.14	0.07	0.07	204.40	540.04	1488.39

Table 6: Computational time spent per block of functions in percent and total time spent for $0.2t^*$ characteristic time in second.

averaged interpolation and spreading operations between the Eulerian fluid mesh and the Lagrangian particles. Therefore, the spatial filtering operations implemented within our work must be improved to reduce the computational cost of the Eulerian-Lagrangian two way coupling.

7. Conclusion

In this paper, a new Eulerian-Lagrangian coupling based on the resolved transport of the interface through a sharp interface capturing method (ICM) and Lagrangian transport for modeling under-resolved droplets for multiscale atomization is presented. The motivation of the coupling is to improve the poor transport of under-resolved droplets in the ICM framework. In this work, a threshold of 4 fluid cells across the volume-based-equivalent diameter is given for our ICM method.

With the present Eulerian-Lagrangian coupling, the transformation from Eulerian droplet toward Lagrangian droplet is done on the same fluid mesh, and thus the Lagrangian droplet is larger than the local fluid mesh. In two way Lagrangian coupling, the spread of the source terms induces a local flow disturbance, accelerating the Lagrangian particle. This results in a poor representation of the forces experienced by Lagrangian droplets, resulting in an inaccurate estimation of the drag force, or worst, a divergence of the solver. The present method circumvents this inaccurate transport of Lagrangian droplets by spatially filtering the particles' momentum across several fluid cells and correcting the local flow disturbance of the particle. The results of the test case studying the free-falling sedimented droplet demonstrate the improvement of the transport of an individual particle regardless of its diameter to fluid mesh spacing ratio.

The criteria of transformation from Eulerian droplet toward Lagrangian droplet, and vice-versa, are meticulously detailed in the present paper, as well as a methodology to track individual Eulerian droplet or ligament. The goal of these criteria is to ensure that the spherical assumption used in the modeling of the transport of droplets is valid. The analysis of each one of the criteria

is necessary because it is computed for under-resolved droplets. In the morphological analysis, this results in an overestimation of the droplet deformation. This must be acknowledged in the choice of the threshold values. Similarly, the methodology to reconstruct the Eulerian fields is also detailed, as well as the algorithms used to implement the transformation in both frameworks.

The coupled methodology is validated among several test cases from the literature. The Eulerian-Lagrangian coupling is then successfully applied to the atomization of a liquid jet in a cross flow configuration. The results using Eulerian-Lagrangian coupling and ICM method have a similar accuracy, but the smallest droplets are conserved in the Eulerian-Lagrangian coupling. However, the proposed Eulerian-Lagrangian coupling freezes the volume of the particles, a secondary break-up modeling must be considered in an extension of this work. Although the Eulerian-Lagrangian coupling conserves and improves the transport of the smallest droplets, to our point of view, this method does not prevent *flotsam* or *jetsam* to occur.

Finally, the computational cost of the liquid jet simulation is slightly reduced with the Eulerian-Lagrangian one way coupling. With the two way Lagrangian coupling, the simulation becomes computationally more expensive. The convolution of the fluid variables at the location of the Lagrangian droplet, as well as the spreading toward the source terms of the momentum equation, are responsible for this increase. The computational cost of the simulation using the two way Lagrangian coupling can be decreased by reducing the length of the compact support of the Gaussian kernel.

Acknowledgments

This work was granted access to the HPC resources of IDRIS, TGCC and CINES under the allocation A0132B1010 made by GENCI (Grand Equipement National de Calcul Intensif) and the CRIANN (Centre Régional Informatique et d'Applications Numériques de Normandie) under the scientific project N. 201 704. The authors would thank the Normandy region for their funding of this research.

Appendix A. Disturbed velocity corrections in the two way Lagrangian coupling

In Section 2.2 the Stokes correction reads

$$\psi_{St}(x) = \frac{1}{2145}\begin{cases} 2145 - 1001x^2 + 910x^4 - 735x^5 + 250x^6 - 33x^7 & \text{if} \quad x \in [0:1] \\ 2145/x - 1001/x^3 + 910/x^5 - 735/x^6 + 250/x^7 - 33/x^8 & \text{if} \quad x > 1 \end{cases} \tag{A.1}$$

and varies with respect to the averaging and spreading kernel lengths with $x = \lambda/\sigma$. The Oseen correction is

$$\psi_{Os}(Re_\sigma) = \frac{9\pi}{4Re_\sigma^3}\left(9\pi\left(1 - \mathrm{erf}(Re_\sigma^3/3\sqrt{\pi})\exp\frac{Re_\sigma^2}{9\pi}\right) - 6Re_\sigma + Re_\sigma^2\right), \tag{A.2}$$

and varies with Re_σ, a Reynolds number based on the length of the regularized kernel function (the characteristic length is the size of the compact support of the Gaussian kernel).

Appendix B. Coalescence detection algorithm

The detection of coalescence events is based on a balance of volume between two successive time steps in a fixed control volume. The droplets in this control volume are identified by $\mathcal{X}_k \neq 0$ for the kth cell in the box, at the current time step and the previous one. Then, the volume of the droplets within this control volume is compared to the current droplet, and, an eventual coalescence is detected if the volume coincides.

The simulation of droplets' coalescence is done to illustrate this algorithm. Both droplets have the same diameter, are located at a normal surface-to-surface distance of one radius, and their velocity is initialized to force a coalescence. The field $\mathcal{X}$ is given in figure Appendix B.1a, before and after coalescence. Before coalescence, the two fields have a unique non-zero label, 1 and 2 for the lower and upper droplets, respectively. At coalescence, only one droplet is identified and former labels are stored for droplets' statistics, as shown in figure Appendix B.1b that shows the temporal evolution of the labels in the domain.

Appendix C. Breakup detection algorithm

The breakup algorithm is based on the field $\mathcal{X}$ and aims to identify the droplet breaking into new droplets. Similarly to the coalescence detection, a control volume is used to identify all droplets in the new droplet vicinity where the volume balance is computed between two

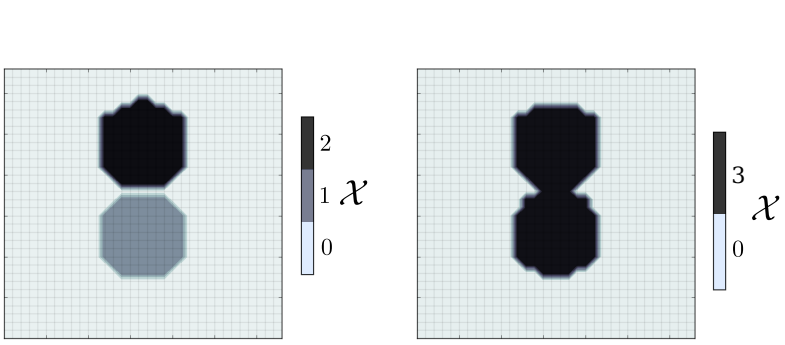

(a) Snapshots of two coalescing droplets represented by their labels.

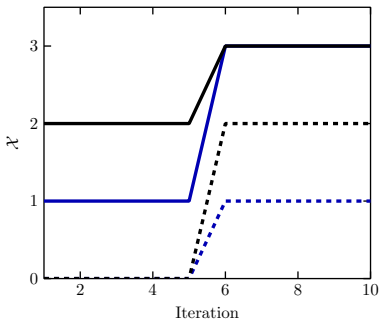

(b) Droplets' label evolution after coalescence.

Figure Appendix B.1: Droplet coalescence.

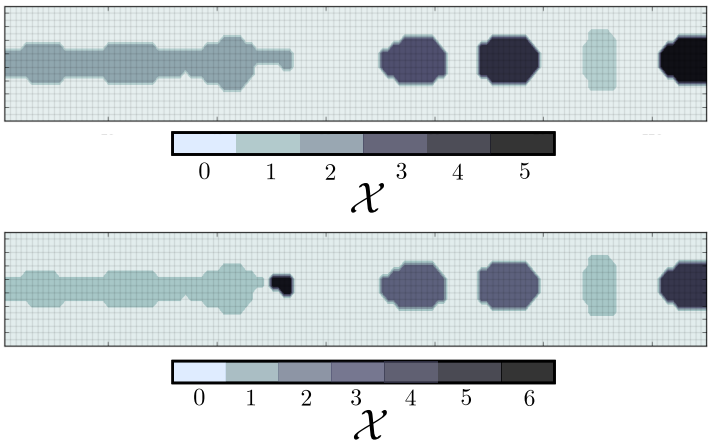

(a) Snapshots of Plateau-Rayleigh simulation where a small droplet is detached from the main liquid core on the left, color bar represents the label of the droplets.

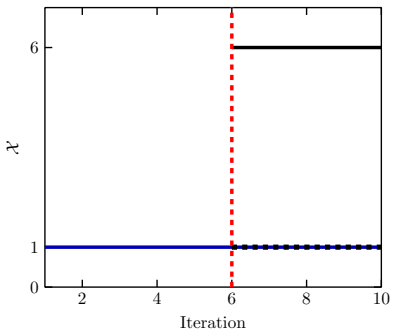

(b) Droplets' label evolution, in blue main core, in black created droplet, and in dashed detached droplet mother.

Figure Appendix C.1: Droplet breakup.

successive time steps. From the knowledge of volume variation the droplets that broke can be tracked to the newly formed droplet.

The breakup algorithm is illustrated through the simulation of the Plateau-Rayleigh atomization, using the numerical configuration of Denner et al. [66]. The simulation consists of the atomization of a pulsed liquid cylinder, which generates a single droplet at its tip. The breakup of the tip of the liquid cylinder into a droplet is shown in figure Appendix C.1a for two successive snapshots. Several droplets are identified with a varying label $\mathcal{X}$. The second snapshot shows the creation of a small droplet near the tip of the liquid cylinder with $\mathcal{X} = 6$. Here, a breakup event is identified through the breakup algorithm, as seen in the temporal evolution of the droplets' label in figure Appendix C.1b (here only the label of the liquid core and the new droplet are shown). At breakup, iteration 5, the new droplet is identified and the label of the breaking droplet is stored.

References

[1] S. Hurwitz, M. Manga, The fascinating and complex dynamics of geyser eruptions, Annual Review of Earth and Planetary Sciences 45 (2017) 31–59.

[2] G. Grant, J. Brenton, D. Drysdale, Fire suppression by water sprays, Progress in energy and combustion science 26 (2000) 79–130.

[3] A. H. Lefebvre, V. G. McDonell, Atomization and Sprays, CRC press, 2017.

[4] G. G. Nasr, T. Söderström, A. J. Yule, L. Bendig, Industrial sprays and atomization: design, analysis and applications, Springer Science & Business Media, 2002.

[5] C. Dumouchel, On the experimental investigation on primary atomization of liquid streams, Experiments in fluids 45 (2008) 371–422.

[6] P. Marmottant, E. Villermaux, On spray formation, Journal of Fluid Mechanics 498 (2004) 73–111.

[7] C. Dumouchel, J.-B. Blaisot, E. Bouche, T. Ménard, T.-T. Vu, Multi-scale analysis of atomizing liquid ligaments, International Journal of Multiphase Flow 73 (2015) 251–263.

[8] M. Gorokhovski, M. Herrmann, Modeling primary atomization, Annual Review of Fluid Mechanics 40 (2008) 343–366.

[9] J. Hasslberger, S. Ketterl, M. Klein, N. Chakraborty, Flow topologies in primary atomization of liquid jets: A direct numerical simulation analysis, Journal of Fluid Mechanics 859 (2019) 819–838.

[10] H.-R. Liu, C. S. Ng, K. L. Chong, D. Lohse, R. Verzicco, An efficient phase-field method for turbulent multiphase flows, Journal of Computational Physics 446 (2021) 110659.

[11] G. Tryggvason, R. Scardovelli, S. Zaleski, Direct numerical simulations of gas–liquid multiphase flows, Cambridge university press, 2011.

[12] E. Schillaci, O. Antepara, N. Balcázar, J. R. Serrano, A. Oliva, A numerical study of liquid atomization regimes by means of conservative level-set simulations, Computers & Fluids 179 (2019) 137–149.

[13] R. Janodet, C. Guillamón, V. Moureau, R. Mercier, G. Lartigue, P. Bénard, T. Ménard, A. Berlemont, A massively parallel accurate conservative level set algorithm for simulating turbulent atomization on adaptive unstructured grids, Journal of Computational Physics 458 (2022) 111075.

[14] D. Fuster, A. Bagué, T. Boeck, L. Le Moyne, A. Leboissetier, S. Popinet, P. Ray, R. Scardovelli, S. Zaleski, Simulation of primary atomization with an octree adaptive mesh refinement and vof method, International Journal of Multiphase Flow 35 (2009) 550–565.

[15] J. Delteil, S. Vincent, A. Erriguible, P. Subra-Paternault, Numerical investigations in rayleigh breakup of round liquid jets with vof methods, Computers & Fluids 50 (2011) 10–23.

[16] T. Ménard, S. Tanguy, A. Berlemont, Coupling level set/vof/ghost fluid methods: Validation and application to 3d simulation of the primary break-up of a liquid jet, International Journal of Multiphase Flow 33 (2007) 510–524.

[17] O. Desjardins, V. Moureau, H. Pitsch, An accurate conservative level set/ghost fluid method for simulating turbulent atomization, Journal of Computational Physics 227 (2008) 8395–8416.

[18] G. Vaudor, T. Ménard, W. Aniszewski, M. Doring, A. Berlemont, A consistent mass and momentum flux computation method for two phase flows. application to atomization process, Computers & Fluids 152 (2017) 204–216.

[19] R. Canu, S. Puggelli, M. Essadki, B. Duret, T. Menard, M. Massot, J. Reveillon, F. Demoulin, Where does the droplet size distribution come from?, International Journal of Multiphase Flow 107 (2018) 230–245.

[20] A. A. Mukundan, G. Tretola, T. Ménard, M. Herrmann, S. Navarro-Martinez, K. Vogiatzaki, J. C. de Motta, Brändle De Motta, A. Berlemont, Dns and les of primary atomization of turbulent liquid jet injection into a gaseous crossflow environment, Proceedings of the Combustion Institute 38 (2021) 3233–3241.

[21] C. Rubel, M. Owkes, Extraction of droplet genealogies from high-fidelity atomization simulations, Atomization and Sprays 29 (2019).

[22] D. Guildenbecher, C. López-Rivera, P. Sojka, Secondary atomization, Experiments in Fluids 46 (2009) 371–402.

[23] M. Herrmann, A balanced force refined level set grid method for two-phase flows on unstructured flow solver grids, Journal of Computational Physics 227 (2008) 2674–2706.

[24] J. Shinjo, Recent advances in computational modeling of primary atomization of liquid fuel sprays, Energies 11 (2018) 2971.

[25] J. Shinjo, A. Umemura, Simulation of liquid jet primary breakup: Dynamics of ligament and droplet formation, International Journal of Multiphase Flow 36 (2010) 513–532.

[26] M. Herrmann, A parallel eulerian interface tracking/lagrangian point particle multi-scale coupling procedure, Journal of Computational Physics 229 (2010) 745–759.

[27] G. Tomar, D. Fuster, S. Zaleski, S. Popinet, Multiscale simulations of primary atomization, Computers & Fluids 39 (2010) 1864–1874.

[28] R. Clift, J. R. Grace, M. E. Weber, Bubbles, drops, and particles, Academic Press, 1978.

[29] D. Zuzio, J.-L. Estivalèzes, B. Di Pierro, An improved multiscale eulerian–lagrangian method for simulation of atomization process, Computers & Fluids 176 (2018) 285–301.

[30] Y. Ling, S. Zaleski, R. Scardovelli, Multiscale simulation of atomization with small droplets represented by a lagrangian point-particle model, International Journal of Multiphase Flow 76 (2015) 122–143.

[31] M. R. Maxey, B. K. Patel, E. J. Chang, L.-P. Wang, Simulations of dispersed turbulent multiphase flow, Fluid Dynamics Research 20 (1997) 143.

[32] P. Gualtieri, F. Picano, G. Sardina, C. M. Casciola, Exact regularized point particle method for multiphase flows in the two-way coupling regime, Journal of Fluid Mechanics 773 (2015) 520–561.

[33] J. Horwitz, A. Mani, Accurate calculation of stokes drag for point–particle tracking in two-way coupled flows, Journal of Computational Physics 318 (2016) 85–109.

[34] F. Evrard, F. Denner, B. van Wachem, A multi-scale approach to simulate atomisation processes, International Journal of Multiphase Flow 119 (2019) 194–216.

[35] T. B. Anderson, R. Jackson, Fluid mechanical description of fluidized beds. equations of motion, Industrial & Engineering Chemistry Fundamentals 6 (1967) 527–539.

[36] J. Capecelatro, O. Desjardins, An euler–lagrange strategy for simulating particle-laden flows, Journal of Computational Physics 238 (2013) 1–31.

[37] S. Balachandar, K. Liu, M. Lakhote, Self-induced velocity correction for improved drag estimation in euler–lagrange point-particle simulations, Journal of Computational Physics 376 (2019) 160–185.

[38] F. Evrard, F. Denner, B. van Wachem, Euler-lagrange modelling of dilute particle-laden flows with arbitrary

particle-size to mesh-spacing ratio, Journal of Computational Physics: X 8 (2020) 100078.

[39] M. Herrmann, Detailed numerical simulations of the primary atomization of a turbulent liquid jet in crossflow, Journal of Engineering for Gas Turbines and Power 132 (2010).

[40] M. Sussman, E. G. Puckett, A coupled level set and volume-of-fluid method for computing 3d and axisymmetric incompressible two-phase flows, Journal of Computational Physics 162 (2000) 301–337.

[41] J. López, J. Hernández, Analytical and geometrical tools for 3d volume of fluid methods in general grids, Journal of Computational Physics 227 (2008) 5939–5948.

[42] M. Kang, R. P. Fedkiw, X.-D. Liu, A boundary condition capturing method for multiphase incompressible flow, Journal of Scientific Computing 15 (2000) 323–360.

[43] J. Zhang, Acceleration of five-point red-black gauss-seidel in multigrid for poisson equation, Applied Mathematics and Computation 80 (1996) 73–93.

[44] L. Schiller, A. Naumann, Fundamental calculations in gravitational processing, Journal of the Association of German Engineers 77 (1933) 318–320.

[45] R. Di Felice, A relationship for the wall effect on the settling velocity of a sphere at any flow regime, International Journal of Multiphase Flow 22 (1996) 527–533.

[46] S. Ghaemi, P. Rahimi, D. S. Nobes, Assessment of parameters for distinguishing droplet shape in a spray field using image-based techniques, Atomization and Sprays 19 (2009).

[47] M. Arienti, X. Li, M. Soteriou, C. Eckett, M. Sussman, R. Jensen, Coupled level-set/volume-of-fluid method for simulation of injector atomization, Journal of propulsion and power 29 (2013) 147–157.

[48] V. Chéron, J. C. Brändle De Motta, G. Vaudor, T. Ménard, A. Berlemont, From droplets to particles: Transformation criteria, in: Proceedings of the ILASS Europe, 29th Conference on Liquid Atomization and Spray Systems, 2019.

[49] R. J. Adrian, Particle-imaging techniques for experimental fluid mechanics, Annual Review of Fluid Mechanics 23 (1991) 261–304.

[50] F. Podczeck, S. Rahman, J. Newton, Evaluation of a standardised procedure to assess the shape of pellets using image analysis, International Journal of Pharmaceutics 192 (1999) 123–138.

[51] V. Chéron, J. C. Brändle De Motta, J.-B. Blaisot, T. Menard, Analysis of the effect of the 2d projection on droplet shape parameters., Atomization and Sprays (2022).

[52] B. Duret, G. Luret, J. Reveillon, T. Ménard, A. Berlemont, F.-X. Demoulin, Dns analysis of turbulent mixing in two-phase flows, International Journal of Multiphase Flow 40 (2012) 93–105.

[53] C. Rosales, C. Meneveau, Linear forcing in numerical simulations of isotropic turbulence: Physical space implementations and convergence properties, Physics of Fluids 17 (2005) 095106.

[54] T. Chen, V. Chéron, Z. Guo, J. C. Brändle De Motta, T. Ménard, L.-P. Wang, Simulation of immiscible two-phase flows based on a kinetic diffuse interface approach, in: Proceedings of the ICMF, 10th International Conference on Multiphase Flow, 2019.

[55] M. Uhlmann, An immersed boundary method with direct forcing for the simulation of particulate flows, Journal of Computational Physics 209 (2005) 448–476.

[56] A. R. Karagozian, Transverse jets and their control, Progress in energy and combustion science 36 (2010) 531–553.

[57] C. Aalburg, B. van Leer, G. M. Faeth, K. A. Sallam, Properties of nonturbulent round liquid jets in uniform gaseous cross flows, Atomization and Sprays 15 (2005).

[58] C. T. Brown, V. G. McDonell, Near field behavior of a liquid jet in a crossflow, in: Proceedings of the ILASS Americas, 19th Annual Conference on Liquid Atomization and Spray Systems, 2006.

[59] M. Herrmann, The influence of density ratio on the primary atomization of a turbulent liquid jet in crossflow, Proceedings of the Combustion Institute 33 (2011) 2079–2088.

[60] F. Xiao, Z. Wang, M. Sun, J. Liang, N. Liu, Large eddy simulation of liquid jet primary breakup in supersonic air crossflow, International Journal of Multiphase Flow 87 (2016) 229–240.

[61] M. Klein, A. Sadiki, J. Janicka, A digital filter based generation of inflow data for spatially developing direct numerical or large eddy simulations, Journal of Computational Physics 186 (2003) 652–665.

[62] M. Pilch, C. Erdman, Use of breakup time data and velocity history data to predict the maximum size of stable fragments for acceleration-induced breakup of a liquid drop, International Journal of Multiphase Flow 13 (1987) 741–757.

[63] P.-K. Wu, K. A. Kirkendall, R. P. Fuller, A. S. Nejad, Breakup processes of liquid jets in subsonic crossflows, Journal of Propulsion and power 13 (1997) 64–73.

[64] X. Li, M. C. Soteriou, Detailed numerical simulation of liquid jet atomization in crossflow of increasing density, International Journal of Multiphase Flow 104 (2018) 214–232.

[65] J. Blaisot, J. Yon, Entropy based image analysis for the near field of direct injection diesel jet, in: Proceedings of the ILASS Europe, 19th Conference on Liquid Atomization and Spray Systems, 2004.

[66] F. Denner, F. Evrard, R. Serfaty, B. G. van Wachem, Artificial viscosity model to mitigate numerical artefacts at fluid interfaces with surface tension, Computers & Fluids 143 (2017) 59–72.